Three-dimensional cometary dust coma modelling in the collisionless regime: strengths and weaknesses

3-D Cometary Dust Coma Modelling in the Collisionless Regime: Strengths and Weaknesses

M.J. Foster[1,2], S.F. Green[2]

[1]Lidar Technologies,
Arctic House Rye Lane,
Dunton Green,
Sevenoaks,
Kent,
TH14 7LD,
UK.

[2]Planetary and Space Sciences Research Institute,
The Open University,
Walton Hall,
Milton Keynes,
MK7 6AA,
UK.

Correspondence to M.J. Foster. E:mail: mfoster@hovemere.com

Abstract

Inverse coma and tail modelling of comets based on the method developed by Finson & Probstein (1968) is commonly used to analyse cometary coma images. Models of this type often contain a large number of assumptions that may not be constrained unless wide temporal or spectral coverage is available and the comets are bright and at relatively small geocentric distance. They are used to predict physical parameters, such as the mass distribution of the dust, but rarely give assessments of the accuracy of the estimate. A three-dimensional cometary dust coma model in the collisionless regime has been developed to allow the effectiveness of such models to constrain dust coma properties to be tested. The model is capable of simulating the coma morphology for the following input parameters: the comet nucleus shape, size, rotation, emission function (including active fraction and jets), grain velocity distribution (and dispersion), size distribution, dust production rate, grain material and light scattering from the cometary dust.

Characterisation of the model demonstrates that the mass distribution cannot be well constrained as is often assumed; the cumulative mass distribution index α can only be constrained to within $\pm$ 0.15. The model is highly sensitive to the input grain terminal velocity distribution so model input can be tested with a large degree of confidence. Complex secondary parameters such as jets, rotation and grain composition all have an effect on the structure of the coma in similar ways, so unique solutions for these parameters cannot be derived from a single optical image alone. Multiple images at a variety of geometries close in time can help constrain these effects.

The model has been applied to photometric observations of comets 126P/IRAS and 46P/Wirtanen to constrain a number of physical properties including the dust production rate and mass distribution index. The derived dust production rate (Q_{dust}) for 46P/Wirtanen was $3\ ^{+7}/_{-1.5}$ kg s^{-1} at a pre-perihelion heliocentric distance of 1.8 AU, and for P/IRAS was $50\ ^{+100}/_{-\ 20}$ kg s^{-1} at a pre-perihelion heliocentric distance of 1.7 AU; both comets exhibited a mass distribution index α= 0.8 $\pm$ 0.15.

Key words: Comets: general, Comets: individual: 46P/Wirtanen, Comets: individual: 126P/IRAS

1. INTRODUCTION

Comets are one of the primary sources of the interplanetary dust complex and may contain material that has been relatively unprocessed since the formation of the solar system. We can generally observe the dust through its scattering of sunlight after its release into the cometary coma. In order to derive physical properties of the dust in the coma and the nucleus itself, we need to model the particle dynamics and light scattering. The dynamics depend on the degree and distribution of sublimation on the nucleus, the nucleus size, shape and rotation state as well as the grain density, shape, composition and mass distribution. The intensity and phase dependence of scattered light also depends on the size distribution, shapes and composition of the grains. Due to the complex interplay between the effects of each of these parameters, it would be impossible to derive a unique solution constraining all of these parameters purely from optical coma imaging, even if a completely representative model could be defined. However, such data are often the only source of information available for the majority of comets, so comparative studies have generally been performed using simplified assumptions (spherical nucleus, spherical dust grains, power law mass distribution etc). Other observations have helped to provide additional constraints for a few comets, such as: thermal infrared imaging and spectroscopy for grain size distributions and albedos, and photometry at large heliocentric distance for nucleus size, shape and rotation.

Space missions provide the possibility of observing individual comets in detail, with imaging of the nucleus and the near-nucleus region, and direct measurement of the dust grains in the coma to derive their mass, density, shape, composition and dynamics. However, all the comet encounters so far have been fast flybys (Table 1) with capability to measure only a few of these properties. Even after the Rosetta mission is completed in the next decade, remote observations and coma modelling will still be the only available technique to characterise the properties of the majority of comets.

The basic shape of cometary comae can be explained by simple fountain type modelling first described by Eddington (1910). As comets enter the inner solar system they are heated and ices on or near the surface sublime releasing gas, which in turn drags cometary dust off the nucleus surface. The dust particle dynamics are dominated by gas drag forces in the inner coma. Further from the nucleus, radiation pressure forces are more important resulting in the typical cometary coma shape. Following pioneering work by Finson & Probstein (1968a, 1968b), this mechanism was used to develop a full cometary tail and coma model that could predict certain physical parameters such as the size distribution of the dust grains and their production rate as a function of time. This technique has been improved by a variety of authors: e.g. Sekanina (1974), Divine (1981), Fulle (1987), with the introduction of progressively increased levels of sophistication. However, certain assumptions have generally remained, such as a spherical non-rotating nucleus, spherical dust grains and symmetry about the Sun-comet line. The basic fountain model and all such models that assess the observable coma such as the one constructed here, model the outer coma where collisions between particles are assumed to be negligible. This is not the case when one examines the comet environment very close to the surface of the comet nucleus, the “inner coma”. This region is too small to be resolved with Earth-based remote sensing and the interaction between the dust and gas has to be modelled hydrodynamically.

In early models such as that developed by Finson & Probstein (1968a) the velocity of the dust ejected into the observable coma was assumed to be zero (although a velocity dispersion was applied to the dust grains within the tail and coma in their model). They were therefore applicable to studies of dust dynamics in the tail. Subsequent models do apply an initial starting velocity to the dust grains. Hydrodynamic models of the inner coma attempt to predict the velocities that dust grains reach within the collisional region and hence the velocity at which they enter the observable coma (e.g. Crifo 1995). Simple 1-D equations have been derived to calculate these velocities (e.g. Delsemme & Miller 1971, Crifo & Rodionov 1997). These are discussed below, but as Crifo &

Rodionov (1997) clearly demonstrate, these are harsh approximations to a real comet as they only hold in certain regions. In order to obtain a realistic velocity profile of the dust entering the *outer* coma a full 3-D inner coma model is required, taking account of variability across the comet surface. The predictions made from the hydrodynamic models for the velocity vectors of the dust entering the outer coma can be tested and evaluated with the model developed in this work.

It is known that comets do not emit isotropically and typically have a sunward biased activity function due to the heating on the Sun facing side of the comet. Fulle (1989) attempts to model the extent of this anisotropic dust emission in the coma. This does, however, introduce another free parameter, hence increasing the difficulty in obtaining a unique solution.

We present a new three dimensional cometary dust coma model in the collisionless region, building on the work of previous authors (e.g. Finson & Probstein 1968a, Divine 1981, Fulle 1987). The first priority for any model should be to fit the observations to constrain the physical properties of the object being modelled. A large amount of flexibility has been built into the model so that more realistic representations of the cometary environment can be included as information becomes available. For ground based observations a number of simple assumptions can be made if no direct observational evidence is available to constrain nucleus properties. The nominal model assumes a uniform spherical non-rotating nucleus with a simple activity function across the comet surface, although it does contain the facility to include complex activity functions, including jets, as well as irregular rotating nucleus shapes. However, the surface actually modelled is not that of the comet nucleus but rather a "pseudo-surface" defined as the point at which the gas and dust no longer interact. The emission functions, dust grain velocities etc are defined at this boundary.

Each physical property affects the shape of a coma to a greater or lesser degree as will be shown. The relative strengths and weaknesses of the model are analysed and assessed so that realistic uncertainties can be associated with the physical quantities that are estimated. Particular attention is paid to the effects of varying the dust mass distribution at the nucleus and the velocity with which the grains enter the outer coma. We assess quantitatively how each of these parameters affects the simulated coma and hence give an estimate of how well a specific solution may be constrained. We also examine how the nucleus properties affect the model output in a qualitative manner.

By using this approach we demonstrate how this and similar dust coma models can be used to constrain a number of physical parameters. However, this will also indicate the limitations of this technique. It is important to understand both the strengths and limitations of the given technique before deriving properties of a given comet. In order to fully characterise a comet in terms of its global parameters (e.g. dust production rate, mass distribution) and localised affects (jets etc), a number of different techniques must be used. For example, observing the comet simultaneously within the IR and visible regions of the spectrum allows the dust production rate and mass distribution to be more precisely constrained, but data obtained at a range of observation geometries cannot provide additional constraints because they will, of necessity be obtained at different times when the activity may have changed. However, for localised affects such as jets and rotation, observations at different geometries can provide additional constraints. For example, Schleicher and Woodney (2003) identify jets within comet Hyakutake by observing the comet close to perihelion at a variety of different geometries. Image processing and models are then used to derive rotation and active area location and to define the point at which some dust particles reach their terminal velocity.

Finally, the comet model is applied to ground based observations of two comets; the original Rosetta target 46P/Wirtanen (ESA, 1993) and comet 126P/IRAS. These represent typical images that may be obtained as part of a large survey and are not of high signal-to-noise or at small geocentric distances. The physical properties of each of these comets including the dust production rate, mass distribution index and dust to gas ratio are estimated, taking into account the assessment of the model's ability to constrain cometary properties.

2. THE MODEL

2.1 General Model Properties

The model is a true three-dimensional simulation of a cometary coma in the collisionless regime. Only this region can be observed from the ground (except for extremely close approaches to the Earth) since the inner coma and the nucleus have an angular diameter of less than an arcsecond. The input source function of the comet is modelled as a tri-axial ellipsoid. For interpretation of observations, where no more detailed constraints are available, and during the majority of the testing of this work, the special case of an isotropically emitting sphere (i.e. uniform activity across the surface on both the night and daytime sides of the nucleus) is used as the baseline. The dust grains are emitted normal to the pseudo-surface of the comet with a size dependent velocity distribution. As they are ejected into space with their individual trajectories, the grains are perturbed by solar radiation pressure, described in the form adopted by Gustafson (1989):

$$F_{pr} = \frac{\overline{Q}_{pr} L_s}{4\pi r^2 c} A_r \qquad (1)$$

where $\bar{Q}_{pr}$ is the mean radiation pressure efficiency factor, L_s is the solar luminosity, r is the heliocentric distance of the comet, c is the speed of light and A_r is the impinging surface area of the dust grain. As the dust is normally assumed to be spherical in nature the impinging surface area, A_r, is normally quoted as πa^2 where a is the grain radius.

The trajectories of the dust particles in the fountain model are determined by their starting velocity (described below) and the radiation pressure force. In reality, the comet is moving through space and therefore the full Keplerian dynamics need to be taken into account if the Sun-Earth-comet geometry has changed appreciably during the time taken for particles to traverse the field of view of the image. This is true for most geometries for the larger grains which can contribute significantly to the observed coma brightness. For testing of the model, the standard fountain model is used, as it is easier to demonstrate the effects of altering the various input parameters being modelled. The effects of using the Keplerian dynamics will be examined and all quantitative results will be reproduced using both methods for computing the trajectories of the particles. In order to calculate the true relative motion of the particles in the cometocentric reference frame, one has to solve the differential equations of motion for the dust grains. Fertig & Schwehm (1984) achieved this with a first order Taylor series expansion. This method is followed here and is detailed in Massone (1987).

One should note that we assume all the cometary dust modelled in this work is of a single composition. For all tests we assume the optical properties of amorphous carbon (Hanner 1983). Other materials that are commonly used are various dirty silicates (Draine 1985), and dirty olivine (Mukai 1989).

For a given material and particle size, the radiation pressure efficiency factor Q_{pr} is calculated over the whole solar spectrum, from which the mean radiation pressure efficiency can be computed:

$$\overline{Q_{pr}} = \frac{\int F_o(\lambda) Q_{pr}(\lambda) d\lambda}{\int F_0(\lambda) d\lambda} \qquad (2)$$

where F_0 is the solar flux. It is the balance between solar gravity and radiation pressure that ultimately decides the path an individual dust grain takes through space. This balance between the forces is described by Finson & Probstein (1968a) for spherical grains:

$$1-\mu=\frac{F_{pr}}{F_{grav}}=\frac{C_{pr}\overline{Q_{pr}}}{\rho_d d} \qquad (3)$$

where

$$C_{pr}=\frac{3L_s}{8\pi cGM_{\odot}} \qquad (4)$$

and G is the gravitational constant, M_o is the solar mass, ρ_d is the density of the dust.

The density of the dust can be assumed to be a constant (as used by Fulle 1987), or it can be assumed to follow a functional relationship such as that used by Divine *et al.* (1986)

$$\rho(a)=3-2.2\left(\frac{a}{a+a_0}\right) \qquad (5)$$

where a is the particle radius and $a_0 = 2$ μm. Interplanetary grains collected by aircraft in the upper atmosphere are observed to be fluffy in nature (Brownlee 1978), made up of agglomerations of sub-micron interstellar particles, and hence their density will be small. In this work we adopt the Divine function, which takes account of the fact that as the grains get smaller they become more compact, and their porosity will diminish.

The starting point from which all the dust is emitted is taken to be the boundary of the inner and outer coma as defined by Crifo (1994). This is the distance at which radiation pressure dominates over the gas pressure acting upon the dust grains

$$r_{circ}=R_N^{eff}\sqrt{\frac{\langle C_d\rangle A_g c\overline{V}}{2\langle Q_g\rangle L_s}} \qquad (6)$$

where R_N^{eff} is the effective radius of the active comet, C_d the drag coefficient, A_g the albedo of the comet, $<Q_g>$ the mean gas production rate of molecules and $\overline{V}$ the mean velocity of the gas (see equation 7). This boundary or pseudo-surface is typically between ten and a hundred times the size of the comet's nucleus. Fig. 1 displays the full geometry of the model. We assume emission from the pseudo-surface in a direction normal to the local surface element and that forces other than radiation pressure do not alter the trajectory. This assumption is not physically valid for the nucleus itself since the true hydrodynamics will alter the particle path. However, we regard the "modelled" nucleus shape to be a combination of the true shape and the inner coma itself (equation 6 is used to calculate the size of the surface). The surface is divided into angular elements of dimension one degree; it is from the centre of these elements that the dust grains are emitted normal to the surface with a given speed. The geometry of the cometocentric frame is constructed such that the x co-ordinate points along the Sun-comet line, the z co-ordinate is along the comet's angular momentum vector, and the y co-ordinate is in the direction of the comet's velocity vector and perpendicular to the Sun direction. To produce a simulated image the scattered light intensity from each grain is summed in a 2-D reference frame (with a specified CCD pixel scale) situated at the Earth's position and perpendicular to the Earth-comet vector.

A flow chart showing how the model is constructed can be seen in Fig. 2. Firstly the comet's geometry, physical properties and position in heliocentric co-ordinates are calculated. The mass distribution of dust is computed and divided into mass bins of equal logarithmic size. The size range used is from 0.05 μm to 1.35 mm divided into 29 bins of equal logarithmic size. The position of each dust grain emitted into the coma is calculated at each time interval. The time interval and the number of time steps must be chosen so that all dust grains have left the CCD field after the full integration time and with time interval small enough to give appropriate resolution. The number of steps and the integration time are adjusted for a given comet to ensure that adequate sampling and integration time are used.

For modelling of ground-based images 1500 time steps is sufficient. The time interval is a

function of the CCD pixel size and grain radius and typically is in the range 500–5000s. This gives a total of over 97 million different grain positions mapped out in space for each grain size forming the simulated coma. The amount of light scattered from the dust towards the Earth and the number of photons striking the simulated CCD are computed.

2.2 Dust Grain Velocity

The speeds of the dust grains as they enter the collisionless region tested here are calculated from work carried out by Crifo & Rodionov (1997) and Delsemme & Miller (1971). Other authors have also produced tools that calculate the terminal velocities within the inner coma (e.g. Wallis 1982, Sekanina 1979, Gombosi *et al.* 1986). The terminal velocity of a given dust grain is defined to occur at the point at which the radiation pressure and the force generated by the expanding gas equalize. Although the grains will not have fully reached their terminal velocity at this boundary because gas drag still has some effect, radiation pressure has a significant influence on the trajectory. We therefore define the boundary of the inner coma, from which the model calculations start, at this point. The region outside this boundary but within which gas drag has some effect is, for most observations of comets, at the limit of ground-based resolution. It is generally assumed that the gas is emitted normal to the surface of the comet nucleus. The resulting expanding shell of gas carries the dust away, so the dust velocity is limited by the gas velocity, which is dependent on the temperature of the nucleus. The mean gas velocity is given by

$$\overline{V} = \sqrt{\frac{8\, k_b\, T_N}{\pi\, \overline{m}}} \qquad (7)$$

where k_b is Boltzmann's constant, T_N the nucleus temperature, $\overline{m}$ the mean molecular mass.

Both of the velocity distributions assessed in the modelling are 1-D equations, which are assumed in this model to be true over the whole nucleus. The first, modified from Delsemme & Miller (1971) is given by Divine *et al* (1986).

$$V_T = 1.8\,\overline{V}\left[\frac{2.37}{\sqrt{1+\delta}+\left(\frac{1.233+3.55\mu_g}{0.9+\mu_g}\right)}\right] \qquad (8)$$

where the dust drag parameter is given by

$$\delta = \left(\frac{2\rho a}{\varepsilon}\right)\left(\frac{16\pi\overline{V}R_N g}{3\overline{m}Q_g}\right)\sqrt{\frac{\pi\gamma}{8(\gamma-1)}}$$

and ε is the efficiency factor at which gas pressure is transferred, γ is the ratio of specific heats, Q_g is the gas productions rate in molecules sec^{-1}, μ_g is the dust to gas ratio (ratio of the dust and gas sublimation rates (Q_d/Q_g), and g is the active fraction. g is a fraction by which the radius of the nucleus should be reduced to account for the fact that not all of the surface area may be sublimating. The effective sublimating area is therefore equal to $4\pi(R_N\, g)^2$. As the value of g is decreased, while all other parameters are unchanged, it has the effect of increasing the terminal velocity because the total gas production Q_g which provides the drag force is concentrated in a smaller area.

The second velocity distribution is a more recent equation formulated by Crifo & Rodionov (1997) with reference to comet 46P/Wirtanen is given by

$$V_T = \frac{W}{1.2+0.72\sqrt{a/a_*}} \qquad (9)$$

where the critical radius is

$$a_* = \frac{\overline{m}(1-A_g)c}{\rho \alpha_s L_s \overline{V}} R_N \frac{f(r)\cos z}{r^2}$$

and the terminal gas velocity is

$$W = \sqrt{\frac{\gamma+1}{\gamma-1}\frac{\gamma k_b T_N}{\overline{m}}},$$

L_s is the latent heat of sublimation of ice, α_s is the coefficient of sublimation, A_g is the dust albedo, *f(r)* is the active icy fraction

$$f(r) = \frac{1}{\left[1+(\rho_I/\rho_d)\Re\right]} \qquad (10)$$

(which is a function of heliocentric distance *r*), ρ_d is the dust density, ρ_I is the ice density and $\Re$ is partial dust to gas ratio. *f(r)* does not refer to the large scale fraction of the total surface area that is icy/active as might be inferred from its name; it is related directly to the localised volume fraction of ice in the surface (*f*=1 for 100% ice surface and 0 for 100% dust surface). It serves a different role in the determination of the terminal velocity than the active fraction (*g*). As *f(r)* is decreased, the terminal velocity is also decreased because the total amount of ice available for sublimation is reduced (it is effectively increasing the dust to gas ratio in the nucleus). $\Re$ differs from μ_g used in equation 8 in that it relates to the local dust to gas ratio in the nucleus material itself in the region of sublimation.

Both of these relations are semi-empirical based on the hydrodynamic model results presented by Probstein (1969). The Crifo & Rodionov equation builds on work carried out by Wallis (1982). It has a number of additional factors over other works (Delsemme & Miller 1971, Sekanina 1979), most notably the inclusion of the active icy fraction of the surface *f*. This parameter allows the velocity profile to be adjusted without changing any other quantities, thus giving greater flexibility. By multiplying the dust drag parameter in the Delsemme & Miller equation by a factor (*g*, the active fraction) the same flexibility can be introduced without altering the form of the equation. Equation 8 can also be adjusted by varying μ_g but this will also change the dust production rate (μ_g Q_g) which is constrained by the luminosity and mass distribution within the comet, and hence is not always desirable. Fig. 3 shows the velocity of the dust computed with two different dust to gas ratios for the Delsemme & Miller function, whereas the active icy fraction (which implicitly changes the partial dust to gas ratio) is varied in the Crifo and Rodionov equation. The gas terminal velocity tends to zero as the grains become large in size and therefore difficult to lift off the surface of the nucleus. In order for the two equations to give similar answers these two parameters must be adjusted accordingly i.e. when *f(r)* is low (~ 0.01) in equation (9) μ_g needs to be relatively high (> 3) in equation (8) unless *g* is varied.

Crifo and Rodionov (1999) point out a more fundamental problem with Delsemme and Miller's work in that the equation lacks a sublimation term, which is a main driving parameter when calculating dust velocities. It is clear that both equations shown here and all similar formulae (e.g. Sekanina 1974, Whipple 1951) are only approximations to the velocities of the dust emitted into the outer coma.

The similar form of the velocity distributions derived from these equations, despite the different mathematical construction, indicates that although the velocity may be constrained with this type of modelling, values of secondary parameters like the active fraction and dust to gas ratio should not be estimated purely from the velocity distributions. Regions where the comet is more active will release dust with greater velocities and thus the velocity of the dust may vary drastically over the cometary surface. True 3-D inner coma models where the hydrodynamics are modelled completely, theoretically should give a picture that is closer to reality when all the nucleus parameters are known.

2.3 Mass Distribution

The mass distribution of the grains is a fundamental parameter that previous authors have predicted for a variety of comets using this type of coma modelling applied to remote sensing, e.g. Fulle (1996). The derived cumulative mass distribution follows the form

$$N(\geq m) = k\ m^{-\alpha} \qquad (11)$$

where N is the number of grains of mass greater than m, k is the mass distribution constant, and α is the mass distribution index. In the simplest representation of a dust mass distribution, equation (11) holds between lower and upper mass bounds m_{min} and $m_{max.}$ These could be chosen such that m_{min} is the mass for which light scattering efficiencies are essentially negligible for the wavelength range of interest and m_{max} is the maximum mass which can lifted from the nucleus by gas drag. The differential mass distribution (i.e. number of grains within a given mass range) is described by

$$dN(m) = -\alpha\, k\, m^{-(\alpha+1)}\ dm \qquad (12).$$

The differential mass distribution index, s=α+1, is often used. From (12), integrating with respect to particle mass between m_{min} and m_{max} the total mass of the dust particles can be found within a given mass range.

$$M = \frac{-\alpha\, k}{(1-\alpha)}\left(m_{\min}^{(1-\alpha)} - m_{\max}^{(1-\alpha)}\right) \qquad (13)$$

For a defined or known mass production rate the value of the mass distribution constant (k) can be computed.

Results from in situ experiments (Table 1) showed that the larger grains dominated the total mass of the dust particles within the comae of three comets. The mass distribution index observed in comet 1P/Halley was not constant with mass; α had four distinct values over the total mass range measured. This measured mass distribution is not, however, the same as that at the nucleus, but the distribution along a path through each comet's coma. It has been speculated that this may be a result of two separate out-gassing periods with different activity levels (Perry *et al.* 1987). Alternatively, Fulle *et al.* (2000) showed that this complex coma mass distribution is consistent with a single slope mass distribution ejected from the inner coma, although the required source mass distribution index was shallow and therefore still dominated by large particles. Large grains were also found to dominate in the second Giotto target, 26P/Grigg-Skjellerup (McDonnell *et al.* 1993) and a three or four component mass index was found by Stardust when it encountered comet 81P/Wild-2 (Tuzzolino *et al*. 2004, Green *et al*. 2004).

In our model the mass distribution is constructed such that each size bin has a range of a factor 1.44 in radius, within which there are grains of various sizes. The velocity and the radiation pressure terms are both dependent on the radius and the mass of the dust. Therefore, taking specific values of mass and radius for each bin produces quantized velocity and radiation pressure values. A random perturbation is applied to the velocity with a Guassian shape of up to $^{+}/_{-}$ 30% of the mean value as computed with either equation (8) or (9) within each bin. This smoothes out the paths taken by the dust and reduces possible artificial features forming in the coma. A similar perturbation is applied to the radiation pressure force impinging on the dust particles.

2.4 Light Scattering

In order to simulate a ground based image of a comet the intensity of light scattering from the dust within the coma must be calculated. It can be shown that cometary comae are optically thin (as reviewed by Jewitt 1991). A variety of light scattering models have been applied to cometary dust, from simple geometric albedo models (Hanner 1983) through to more sophisticated techniques such as the Discrete Dipole Approximation (DDA) (Purcell & Pennypacker 1973). The most common technique used is Mie theory as described in detail by van de Hulst (1957). However, Mie theory has only been solved for certain special cases i.e. spheres or infinite long cylinders. This fact has led

to the development of techniques such as DDA which in theory can simulate any dust grain shape. However, laboratory experiments using microwave analogues of rough and complex particles (Gustafson et al. 1999) have shown that, despite the assumption of using spherical dust grains, Mie theory provides a good approximation to reality. For this reason Mie theory has been used for the simulations described within this paper although the results of any light scattering technique can be included within the model to compute the intensity of light observed at the Earth. Mie theory is also used to calculate Q_{pr} for grains of various sizes and composition (see Fig. 4).

First computed by Mie in 1908, the intensity of light scattered in a given direction, $F(\theta)$, is

$$F(\theta) = \frac{1}{2k^2}\left[|s_1(\theta)|^2 + |s_2(\theta)|^2\right] \qquad (14)$$

where the scattering matrices are

$$s_1(\theta) = \sum_{n=1}^{\infty} \frac{2n+1}{n(n+1)} \{a_n \pi_n(\cos\theta) + b_n \tau_n(\cos\theta)\}$$

$$s_2(\theta) = \sum_{n=1}^{\infty} \frac{2n+1}{n(n+1)} \{b_n \pi_n(\cos\theta) + a_n \tau_n(\cos\theta)\}$$

a_n and b_n are the scattering coefficients, $k=2\pi/\lambda$, (λ is the wavelength of the light), π_n and τ_n are terms dependent on Legendre polynomials.

Mie theory has been solved here for spheres only, as it is extremely difficult to obtain converging solutions for more complex shapes. As the dust grains become much larger than the wavelength of light, convergence problems occur and computing time increases dramatically. Eaton (1984) applies an approximation (Kattawar & Plass 1967) which permits Mie scattering calculations for grains of up to approximately 10000 times the wavelength of the light.

Mie theory calculates exact results for a spherical dust grain of a given composition and size, at a defined scattering angle and wavelength. It produces highly pronounced artefacts due to high order oscillations in the results either for scattering intensity phase curves (intensity versus scattering angle for a single grain size) or for intensity as a function of grain size at a single scattering angle. To reduce the effect of such artefacts the Mie theory results are smoothed over a small size range (the width of the size bin in the model) and weighted according to the shape of the size distribution used.

The effect caused by the assumption that all of the dust grains are spherical in nature and of a single bulk density, is reduced by the random perturbation that is applied to the velocity of the particles and the radiation pressure they experience. The dust grains in reality are likely to have a range of different shapes and sizes and the perturbation is an attempt to reflect this. The spherical grain assumption still affects the calculations for the scattering of the light by the dust coma but it does not influence the derived coma images to the same extent as many other uncertain factors (e.g. grain velocity or mass distribution).

2.5 Nucleus Properties

A range of properties have been observed or deduced for a number of comets, such as rotation (e.g. Meech *et al.* 1997, Keller *et al.* 1987), dust concentrations within the coma commonly called jets (Thomas & Keller, 1987), and uneven activity across the comet surface particularly in the sunward direction. Data from comet flybys have shown that cometary dust comae exhibit a great variety of structures that cannot be observed from the ground, including narrow jets (e.g. Soderblom *et al*. 2004; Sekanina *et al.* 2004) and fans (e.g. Thomas & Keller 1987). All of these features can be modelled.

Rotation of the model comet nucleus requires the appropriate transformation matrix to be

used in a time dependent manner, such that the nucleus can rotate about any axis and at any rate. Jets can be generated by increasing the activity of a region on the nucleus surface above the surrounding area. This may be done in a harsh manner (i.e. with a sudden increase from one part of the nucleus to another) or with a smooth function (e.g. McBride *et al.* 1997). The uneven activity across the comet surface may be produced in a number of ways, e.g. by defining a number of active regions across the whole surface or by defining gross anisotropies. Sunward anisotropies can be simulated using a form of cosine functional dependence from the sub-solar point (or displaced due to thermal lag) on the nucleus. Different functions have been used in earlier comet models (generally in 2-D models or symmetric 3-D simulations) such as 5-3cos(θ) (where θ is the angle from the sub-solar point, Divine 1981), or some other simple cosine dependence (Crifo 1995, Fulle 1989). In this paper two different anisotropies are applied in order to demonstrate the effects of having the majority of the dust emitted in either a 45^0 cone (using a $\cos^2(2\theta)$ activity function) or a 90^0 cone (using a $\cos^2(\theta)$ activity function) towards the Sun. Both of these activity functions leave the dark side of the comet completely inactive, which is convenient when demonstrating the effects of a sunward bias activity function. However, in a real comet such a cut would be surprising and some activity may well exist on the dark side so the Divine (1981) function may be more applicable.

3 TESTING AND RESULTS

3.1 The Basic Simulation

So that the relative effects of the various input parameters could be tested systematically within the coma model, a test comet and the observer (usually the position of the Earth) are placed at a convenient position in space. The comet is initially placed in the ecliptic plane and the observer is set at 1 A.U. from the Sun along the x-axis in heliocentric co-ordinates (at the autumnal equinox). The comet is then positioned such that the Sun-Earth-comet angle is 90^0. Thus the comet has a heliocentric distance of 0.94 AU and geocentric distance 0.34 AU

The dust production rate is one of the main input parameters that we are trying to constrain. It is directly proportional to the luminosity of the cometary coma. However, it is also embedded within the velocity calculations of the dust grains before they enter the collisionless regime. For the purposes of testing the cometary model the mass production rate is kept constant at 100 kg s^{-1}. This prevents the velocity being perturbed by adjusting the brightness of the comet. The mass production rate of the dust is not the only input parameter that has an effect on the luminosity of the comet; the mass distribution also affects the coma brightness. The relationship between the mass distribution index α and the modelled luminosity (light scattered by dust within the R filter) of a cometary coma is shown in Fig. 5 for dust grains of a single composition (amorphous carbon) with a fixed production rate. Using a different dust grain composition, the absolute values are altered but not the shape of the graph. This leaves us with three inputs (dust production rate, grain material, and the dust mass distribution) that have a noticeable effect on the absolute R band magnitude of the cometary coma. The way in which dust grains of various sizes influence the luminosity from the coma can be seen in Fig. 6. This displays the amount of light reflected by grains in each mass bin towards the observer for various values of the mass distribution index. The range of cases displayed (alpha between 0.4 and 0.8) shows the relative importance of different grain sizes to the observed coma. For α = 0.8, the small grains dominate the scattering and for alpha equal to 0.4 the large grains are dominant (if the light scattering were purely geometric then α = 2/3 would result in equal scattering areas for all size bins). The functions for alpha equal to 0.6 and 0.7 show that grains of all sizes play a significant role at these mass distribution indices. When the surface area of the grain is approximately equal to the wavelength of the light, the scattered light increases above the trend, which is a result of the increased Mie scattering efficiency.

The terminal velocities, by definition, are applicable at the boundary of the inner coma

region (calculated using equation (6)). The size of this region has little affect on the final result as it is negligible compared with the size of the collisionless coma or the resolution of any ground based images. The nucleus/inner coma shape however does drastically alter the starting normal vectors, and therefore the profile of the coma, as will be shown later.

All simulations here have used amorphous carbon grains. Other materials that could be used, such as dirty silicates (e.g. Draine 1981), would alter the values of the radiation pressure efficiency factor and the light scattered by the dust grains. This fact gives an indication of how many free parameters there are and therefore how difficult it is to obtain a truly unique solution without additional constraints.

Therefore "nominal" model construction assumes a dust production rate of 100 kg s^{-1}, mass distribution index of 0.8, uses equation 8 to calculate the velocity with μ = 1.5 and g = 0.5, a pseudo-surface with a diameter of 10 km, isotropic emission function, with no rotation and amorphous carbon dust grains.

3.2 Mass distribution

In order to investigate the effect of the mass distribution index (α) on the comet model output, the nominal simulation is constructed as described above, with only α adjusted. Fig. 7a-c show the resulting model output for the fountain model displayed as a contour map with input α values of 0.4, 0.6 and 0.8 respectively. The difference between each of the plots is not very substantial, showing that the shape of the model output is not highly sensitive to the value of α. To demonstrate this, a quantitative measure of the variation is required. Therefore all synthetic coma intensities were normalised and compared with the contour map obtained when $\alpha = 0.8$. The relative χ^2 values are then calculated as α is adjusted. Fig. 8, which shows the χ^2 values plotted as a function of α, demonstrates that when the smaller particles dominate the total surface area of the dust ($\alpha >$ 0.66), changing the mass distribution does have a noticeable effect on the shape and profile of the simulated comet coma. For $\alpha < 0.66$ the gradient of the χ^2 plot reduces, demonstrating the difficulty in distinguishing between different mass distributions with a large degree of accuracy from the ground when large grains (for which the grain velocities are similar and low) are highly dominant.

3.3 Velocity

Keeping the mass distribution and all nucleus parameters constant, the influence of the grain velocities on the model output can be examined directly. Adjusting the velocities of the dust grains has the effect of altering the distribution of the dust particles throughout the coma. We can adjust the velocity distribution defined by equation (8) by changing the dust to gas ratio (Note that the velocity distribution can be adjusted by a range of parameters). It should also be remembered that there is a random perturbation placed over this velocity for a given particle size of up to ± 30%, so it is therefore the mean velocity of grains of a particular size we are trying to constrain.

Fig. 9a-c shows three different contour maps with dust to gas ratios of 1, 2 and 3 respectively, which translate to the mean velocities for 0.1 mm grains of 58, 39 and 31 m s^{-1}. Large changes in the shape of the model output can be seen, indicating that the model is highly sensitive to the input velocity. The variation in χ^2 is shown in Fig. 10, which is computed relative to the contour map obtained when the dust to gas ratio is 1.5.

The model output shows a similar sensitivity when the velocities are calculated with equation (9) as shown in Fig. 11a-c. This equation is adjusted using the parameter f. The values of f used were 0.01, 0.03 and 0.05. These values of f correspond to velocities of 12, 20 and 26 m s^{-1} for 0.1 mm grains. The dust to gas ratio is buried within the f parameter (equation (10)). However, it should be noted that Crifo (1995) does show that the velocity is dependent on the local dust to gas ratio not the global value. The sensitivity of the model to the input velocity displayed by both

functions implies that this can be well constrained. The differences between the simulations, using the various values of f in equation (8) are displayed quantitatively as a χ^2 plot in Fig. 12 (the simulation with f=0.01 is used as the nominal result with which the others are compared).

3.4 The Orbital Dynamics

Including the full orbital dynamics (i.e. the heliocentric Keplerian motion, modified by radiation pressure, as with the fountain model) does alter the shape of the simulated cometary coma as shown in Fig. 7d-f and Fig. 9d-f. The affect of including the cometary motion is more dramatic when the large grains dominate the light scattered towards the Earth.

Fig. 7d-f is produced with the same inputs used in Fig. 7a-c but with the orbital dynamics included. As with the fountain model the χ^2 values are calculated to give a quantitative measure of the relative variation between each model (Fig. 8). Fig 8 demonstrates that the result produced using the fountain model is replicated when the orbital dynamics are included. The affect of varying the velocity on the full orbit model is shown in Fig. 9d-f alongside the model outputs produced using the basic fountain model. The *relative* change in model output when the orbital dynamics are included is the same as that found with the fountain model; the χ^2 values are displayed in Fig. 10. These results indicate that although the orbital dynamics should be included when simulating a cometary coma because the overall shape does change, testing of the model characteristics and sensitivities to input parameter variation can be performed using the fountain model which produces the same *relative* variation.

3.5 Nucleus properties

The nucleus properties of a comet affect the coma shape in a variety of ways. Due to this variability of potential emission functions, a quantitative measure of the effect of the nucleus shape on the coma sheds little light. The affect of the nucleus shape on the model is therefore discussed in a more qualitative manner. The first shape simulated is an anisotropy in the dust emission, biased towards the Sun. It is also logical to assume that the Sun-facing side of the comet will have greater activity as this is the side being directly heated. Fig. 13a-c show $\cos^2(\theta)$, $\cos^2(\theta/2)$ and $5\text{-}3\cos(\theta)$ sunward biases respectively, where θ is the angle from the solar direction. The shapes of the contour maps produced are clearly different to those created with isotropic emission. The width of the coma becomes relatively larger compared with the width of the tail as the sunward cone narrows. The change is much less noticeable using the $5\text{-}3\cos(\theta)$activity function (shown in Fig. 13c). It is this and similar emission functions which are more likely as activity is expected to be reduced and not eliminated on the comet's dark side. Although direct sublimation from the unilluminated surface of cometary nuclei is unlikely, the initial non radial gas flow close to the nucleus can cause dust terminal velocities apparently originating from the dark side in hydrodynamic models (e.g. Crifo & Rodionov 1997). If the activity originates below the surface, then dark-side emission is more likely (e.g. as seen in comet Wild 2)

In some comets a sunward bias of emission can be observed quite clearly from the ground. Predicting the exact shape of the cone for this and similar models is rather difficult if there is no clear direct observational evidence. Examining the model outputs produced in Fig 13a-c it is estimated that the size and shape of any sunward bias cone in the nucleus activity function can only be constrained within $\pm 30^0$. It should be noted that if a range of geometries are examined it may be possible to constrain this angle to a greater degree than the level quoted here.

The other main variation of activity across the surface of the comet could be in the form of jets or concentrated active regions. Jets were clearly seen by Giotto (Thomas & Keller 1987) on comet P/Halley and more recently by Stardust on 81P/Wild 2 (Sekanina *et al.* 2004) and by Deep Space 1 on Borrelly (Soderblom *et al.* 2004), although what causes them is a matter of some debate.

Jets have generally been assumed to emanate from active areas on the surface of the comet (e.g. Sekanina 1986). Enhancement of ground-based images shows structures that move through the coma. If one assumes that an active area generates the jet and that this is not perturbed other than by radiation pressure, the rotation can be calculated (Whipple 1982, Sekanina 1986). This technique is difficult to apply to Earth based images unless the comet is close (to obtain reasonable spatial resolution), bright (to ensure that the sometimes low-contrast structures can be identified against the overall coma, and sufficient temporal coverage is obtained to track the jet evolution. Owing to the large number of parameters required to interpret the data (and the complexity of jet structure observed in comet flybys) the technique does not generally allow demonstration of the uniqueness of the derived set of parameters (Jorda & Gutiérrez 2002). However, it has been successfully used to infer rotation axis orientation and rotation rate for a number of bright comets (although rotation rates are more often and more straightforwardly derived from nucleus light curves when activity is low). Hydrodynamic models of the inner coma (e.g. Crifo 1995) have shown that jets can be created by shocks in the gas flow in this region, and therefore the movement of the jet could be related to hydrodynamic activity near the nucleus surface as well as activity on the surface itself. However, the spatial density variations apparent from in-situ measurements (e.g. Green *et al.* 2004) imply far greater concentrations of dust than such models predict (e.g. Rodionov *et al.* 1999). Whatever the mechanism for their production, there is now observational evidence to support the existence of significant concentrations of dust in narrow jets, at least in the near nucleus region.

Fig. 14a shows the results of a model with a single jet being emitted from a single point (one degree surface element) on the surface with an activity a hundred times that of the surrounding area. There is very little effect on the final model output and the jet can only just be identified without image processing. Fig. 14 b & c were generated with a jet from the same point as in Fig. 14a but with activity at 1000 and 10000 times above their surrounding environment. Although single jets at these higher activity levels completely dominate the coma shape, they are not usually evident in large scale ground based coma images. Even though such high spatial density concentrations are found in in-situ data at 81P/Wild 2 this is interpreted as due to local particle fragmentation (Green *et al.* 2004, Clark *et al.* 2004). Such structure in the inner coma is smeared out by dispersal of the fragmentation clouds into a larger scale background. In addition, the inner coma is characterised by a large number of narrow jets which will also be averaged out at large scales.

The effects of using an elliptical pseudo nucleus surface with different orientations can be seen in Fig (15a-c). As cometary nuclei are most likely irregularly shaped an ellipsoid nucleus will usually be a better approximation than a sphere. The results shown in Fig (15 a-c) show that shape and orientation of the input function can have a dramatic effect if you assume that all the grains are ejected normal to the surface. If the larger axis in the ellipsoid is orientated in the x-y plane, the artefacts that are produced are very similar to those produced by jets (Fig. 14a). Fig. 15c displays a highly elongated image when the ellipsoid is stretched perpendicular to the x-y plane. These results demonstrate a high degree of sensitivity in the model to the input normal vectors, which can cause prominent artefacts within a simulation. This does not however demonstrate necessarily that the nucleus shape affects the coma structure, because the dust grains are likely to be emitted in a number of different directions from a single point on the cometary body and not only normal to the local surface as assumed here.

The results of rotating the comet in space are shown in Fig. 16a-c. In order to show the effects of rotating the nucleus clearly, the isotropically emitting nucleus functions as used in the two simulations shown in Fig. 14a &14b are rotated. The nucleus is rotated about the comet's z-axis at a rate of one rotation per 24 hours in Fig 16a-b and about the y axis in Fig 16c. The rotation has affected the model output with Fig 16b showing the greatest change caused by rotation as one might expect. A more complex rotation could be performed than the one demonstrated here, but it is evident from this simple rotation that the results are difficult to distinguish from other effects and therefore the rotation itself is very difficult to constrain with this technique alone. At the very least a good time series of images would be required with clearly observable structure within the coma.

Rotation rates of comets have been determined using photometric light curves at large heliocentric distance (e.g. Meech *et al.* 1997) or coma features (e.g. Whipple 1982, Sekanina 1986). Some objects, including 1P/Halley (Belton *et al.* 1991) exhibit complex rotation.

4 APPLICATION TO COMETS 126P/IRAS AND 46P/WIRTANEN

4.1 Observations

Observations of comets 46P/Wirtanen (the proposed target for the ESA Rosetta mission at that time) and 126P/IRAS were taken on the 10th and 11th November 1996 at the 1m telescope of the South African Astronomical Observatory (SAAO) (Table 2). Both these objects represent typical faint comets that might be observed in a large scale survey programme. Data were also taken on the 9th of November but were of poor quality due to bad weather conditions and telescope tracking problems at the time of observation. A TEK CCD of 512×512 pixels was used at the f16 Cassegrain focus, each pixel having a field of 0.35 arcsec. Observations were taken in the standard Johnson-Cousins VRI filters (λ = 550, 650, and 830 nm). In both cases the model is applied to the observations taken in the R filter as these have the highest signal to noise and are relatively uncontaminated by gaseous emission. Seeing was stable throughout both nights at approximately 1.6''. Due to telescope tracking limitations no single observation was taken with an exposure time of longer than 300 seconds.

All the images were bias corrected and flat fielded in the standard manner. The comet images were coadded for each night in order to obtain better signal to noise. Although this removed any information that may have constrained the rotation of the comet, it permitted the fitting of contours at lower intensity levels. All the reduction was performed with Starlink software packages KAPPA, GAIA and FIGARO.

In order to coadd the images the following procedure was followed: Firstly the background sky intensity (defined by the mean background close to but outside the coma of the comet) was removed, as well as any bad pixels or cosmic ray hits. Any stars that entered close to the field of view of the observed comet were removed from the frame before the comet images were coadded. If the star was embedded within the coma, either partially or fully, the frame was discarded. The final coadded comet frame was then normalised such that the mean pixel value was equal to one. The Photometric results of these observations can be found in Epifani *et al.* (1999).

4.2 Model Application

All the tests of the model carried out thus far did not involve real data. 126P/IRAS displayed a broader and brighter coma than 46P/Wirtanen and the model is therefore applied to this comet first. The model is applied to both comets in a systematic manner as described below. The velocity of the dust was calculated with the adjusted Delsemme & Miller fit (equation 8), although any similar function can be used without altering the model application process.

An initial estimate is made of the dust production rate; both of the comets observed have a relatively low level of activity and thus the dust production rate was estimated to be 100 kg s^{-1}, in both cases. All the nucleus parameters were initially assumed to be simple, i.e. the nucleus is spherical, non-rotating and isotropically emitting. It should be noted that even if data existed indicating a non spherical nucleus the input source function should still be assumed to be spherical in the first instance. If observations clearly demonstrate rotation of jets or other such parameters at the inner-outer coma boundary this should be taken into account after the simple simulations are processed. The dust composition is then chosen; for both comets modelled in this work the composition was assumed to be equivalent to amorphous carbon. The light intensity and the radiation pressure efficiency factor are then calculated using Mie theory. This leaves two major dust

parameters, the mass distribution of the dust and the particles' starting velocities, to be varied in the model.

Initially, 12 simulations are carried out with mass distribution indices α from 0.5 to 0.8 in increments of 0.1 with three different velocity profiles. While using equation (8), the active fraction g was set equal to one and the dust to gas ratio μ was adjusted from 1 to 3 in equal increments. Although it was shown that the velocity can be relatively well constrained to within a dust to gas ratio ± 0.25, for the first series of simulations it is desirable to get an approximate idea of the best fit. The resulting model outputs are normalised in the same way as the data, so that the images may be directly compared. If two of the velocity profiles give good solutions with a set mass distribution then the velocity can be narrowed down. In the case when none of the models have produced good fits the search is widened. Faster grains should be used if the real comet displays a broader shape than the model, and slower grains if the opposite is true. A higher mass distribution index e.g. α = 0.9, may be used if it is clear from the early simulations that the small grains are dominant within the coma, but only with the velocity distributions that have been seen to give the best quality fits. Once good nominal fits (judged by eye) have been achieved with the simple source function, the model may be rerun with the 'best' dust parameter inputs and a sunward bias source function. If introducing a sunward dominant source function reduces the quality of fit obtained, an isotropic function is assumed.

Once reasonable fits have been obtained that display the general shape of the comet, a χ^2 calculation is used to compare quantitatively the simulations. However, before the χ^2 values are computed the central pixel of the model outputs was removed as this can distort any χ^2 calculations. This pixel is artificially bright in the model output because, in the observed data, the central area is convolved with the atmosphere and the telescope optics. The global χ^2 should only be used as a guide when judging the best results as it can easily be distorted by bad pixels in the data. Additionally, χ^2 analysis can place a disproportionate emphasis on the central contours due to their greater luminosity. Therefore the top two or three χ^2 results should be taken forward as the nominal solutions and then personal judgement as well as the statistical χ^2 should be used to decide the best fit. The χ^2 measurement of individual isophotes can also be looked at to help determine the best solution.

If no good fit has been obtained, more complex emission function parameters may be invoked, although this has the knock-on effect of immediately reducing the uniqueness of the solution. Unless other evidence exists for including additional factors, e.g. a jet, it would be prudent to avoid attempting to obtain solutions with these and the other complex inputs.

Once the best fits to the data have been achieved the model's intensity within a given aperture is computed. As the dust production is directly proportional to the luminosity it can be adjusted to obtain the desired level of intensity. This would, however, imply a change of velocity, as the mass production rate of dust is embedded in one of the velocity equations (8). However, this can be readjusted by altering any number of parameters within the equation. If the dust production is required to be lower than the original estimate (which will lower the dust velocity), then lowering the value of g (the active fraction) can counteract the effect. If the dust production rate is required to be higher, which increases the velocity of the dust, one can for example increase the size of the nucleus (within sensible limits), to bring the velocity back down to the required level. If, however, equation (9) is used to calculate the velocity, the dust production is replaced by sublimation terms, which are fixed and therefore the mass loss rate of dust has no affect on the grain velocities.

Naturally if any other parameters are constrained by other observations such as the nucleus size and shape these should be taken into account and used in the initial model inputs.

4.3 126P/IRAS

Fig. 17 shows the observed contour map of comet 126P/IRAS produced from coadding 11

images. The good signal to noise provides very clear, well defined contours spanning tens of thousands of kilometres. Before the images were coadded three stars had to be removed from several of the CCD frames. The coma of the comet never passed over the stars but they were close enough to the outer-boundary to possibly reduce the clarity of the outer-most regions of the coma

The inner contours in Fig. 17 are extremely well defined whereas the low signal to noise is apparent in the outer contours. The coma appears symmetrical with no obvious clearly defined features or structures present. Displayed in Fig. 18 are all the model simulations, overlaid on the observed contour map of comet 126P/IRAS. All have isotropic emission and a dust production rate of 100 kg s^{-1}, a spherical non-rotating nucleus with a 1 km radius and an inner coma boundary ~ 50 km in size. It is immediately evident that the models that used low mass distribution indexes ($\alpha <$ 0.66), where the big grains dominate the surface area, have produced the poorest quality fits. It is also clear that the model outputs that use a dust to gas ratio $\mu_g = 1$ produce a dust velocity that is too fast in the majority of the simulations. For the slowest velocity profile used (μ_g =3) the majority of simulations also appear quite poor except for those with a mass distribution index $\alpha \sim 0.8$. The χ^2 values of all these simulations are shown in Table 3. The general trends observed with the eye are confirmed by the χ^2 values except that the fits clearly seem best with $\mu_g = 2$ and that μ_g =1 gives better solutions than when it equals 3. A closer examination is required of the simulation with $\alpha =$ 0.8 and μ_g =3 to investigate this difference.

Examining Fig. 18 l in detail ($\alpha = 0.8$ and $\mu_g = 3$) the reason for the discrepancy in the judgement of the quality of fit, between the χ^2 measurement and that made with the eye becomes clear when the individual contours are examined. The well defined middle contours corresponding to magnitudes 22.18, 22.78, 23.38 per square arcsecond draw the eye by the quality of the fit in this region. However, if one concentrates on the boundary at the front of these isophotes it is clear that the quality of the fit is reduced here. For the outer most contours displayed it is evident that the simulations do not reproduce the data accurately.

Also shown in Fig. 18 l is the apex boundary from the model simulation corresponding to a magnitude 30. No dust grains travel beyond this point in the model. The apex cannot be seen in the real data as its intensity is too low and thus blends into the background and therefore is not displayed in the majority of fits produced. If it was possible to observe this apex boundary the simulations should be fitted to the apex first. If the model apex is within the outer most observed contour of the comet the simulation will not be representative of reality.

Therefore the model apex should be confirmed to be at or beyond the outermost observed contours in the data. Additionally the faintest model contours should have a lower intensity than the weakest observable isophotes in the data. If the intensity level is higher in the model apex than the outer contours in the data, the simulation is not representative of the comet and should be discarded. This indicates that χ^2 measurement is indeed a useful tool for judging the best fit to the data.

Fig. 18n displays a simulation with $\alpha = 0.9$ and $\mu_g = 2$, yielding a global χ^2 of 4784. Looking at Fig 18n one can see that increasing the velocity should improve the fit to the data; this is indeed the case but it does not improve the fits beyond the quality produced from those simulations with α =0.8 and μ_g = 1-2. Fig 18m displays an additional simulation with $\alpha = 0.8$ and $\mu_g = 1.5$, giving a χ^2 value of 3702, the lowest achieved. The three best fits from the global χ^2 are achieved with α = 0.8 and μ_g =1, 1.5, 2. It should be noted that with a mass distribution index of 0.7 good fits are also achieved but all of consistently slightly lower quality.

The eye tells one immediately that the fit with μ =1 is the poorest of the three, producing a shape which is much too broad and with an apex beyond the tip of the comet head. It was decided not to use a different source function with sunward anisotropies because results described above show that these would reduce the quality of the fit (particularly for the outer contours) by tightening the isophotes in this region. Of the remaining best fit simulations it is evident when examining by eye that the simulation with $\mu_g = 2$ gives the better result for the well defined middle contours than when $\mu_g = 1.5$, contrary to the global χ^2. This is because the outer contours are broader and more

flared than their inner counterparts, displaying a different shape which is better fitted with faster grains. For the inner most contours within the middle 20 × 20 pixels, both of the simulations are of similar quality. For the central, well defined contours (those with magnitudes between 22.2 –24) the velocity profile with $\mu_g = 2$ returns the best fit; this is not the case for the outer contours. As the signal lowers so the widths of the outer contours become broader and their importance can be over-weighted in a χ^2 measurement. Also, the background sky level can affect the shape of the outer isophotes as the SNR falls. As the signal lowers, the undulations in the background sky have a greater affect on the contours.

The best fit solution has therefore been shown when $\mu_g = 2$. With this value constrained it is possible to calculate the mass production rate of the dust. Upon comparing the luminosity of this image before normalisation to that measured for comet 126P/IRAS, a mass production rate of 50 kg s^{-1} is obtained. This leaves us with the following solution to the coma properties of comet 126P/IRAS:

- $\alpha = 0.8 \pm 0.15$ (for particle masses in the range 10^{-20}-10^{-4} kg)
- The velocity of a 1 μm and 0.1 mm grain entering the outer coma is 55 m s^{-1} and 10 m s^{-1} respectively. Using equation (8) this is obtained with a dust to gas ratio $\mu_g = 2 \pm {}^{0.33}/_{0.5}$ and an active fraction $g = 0.5^{+0.3}/_{-0.2}$ assuming a 1 km radius nucleus, or with a $f = 0.05$ with equation (9).
- Dust production rate $Q_{dust} = 50^{+100}/_{-20}$ kg s^{-1},
- A source function without a strong sunward anisotropy.

The error bars placed on the mass distribution are on the conservative side taking account of the results shown in Fig. 8. The mass production rate of the dust is highly dependent on the mass distribution that is used. This means that estimates of Q_{dust} will always have large uncertainties.

Thermal observations of this comet carried out by Lisse *et al.* (1999) in mid October 1996 show that small grains dominate the dust. They calculate the production rate to be of the order 300 kg s^{-1} using a mass distribution based on that returned by Giotto (McDonnell *et al.* 1991) in the range from 10^{-20} – 0.1 kg. This is in approximate agreement with the values computed here. If the GIOTTO mass distribution is used within the simulations carried out in this paper the dust production rate would increase to 400 kg s^{-1} due to the extended range. Increasing the range of the mass distribution to 10^{-20} – 0.1 kg does not affect the shape of the final model output because the optical scattering is very insensitive to this large grain mass distribution above 10^{-6} kg although the large grains do make a significant contribution to the mass output. This illustrates the importance of quoting the particle mass limits used when determining the mass production rate.

Additional factors could be introduced into the model to improve the quality of the fit produced. Mechanisms that can be invoked are fragmentation or sublimation of the dust to fit the outer regions, or a changing activity function, i.e. having the comet more active in the past. To fit the inner region of the comet, a simple reduction of activity could be used at the desired position in the source function. However, one must be careful not to introduce too many parameters which merely result in non-unique solutions.

4.4 46P/Wirtanen

The images of comet 46P/Wirtanen were very faint and therefore the contour map obtained from the data (Fig. 19) was of low quality. In order to obtain this map, the final coadded image was binned, (3 × 3 pixels) increasing the signal to noise but reducing the resolution. The 46P/Wirtanen frame is only 71 pixels square compared with the 130 pixel square images used for 126P/IRAS. Two stars were removed from the original images in the manner described in section 4.3. There are a few small objects in the Wirtanen frame that were not removed due to concerns that this would introduce false results because of their proximity to the coma. The removal of the frames that they are present in has a severe affect on the total signal to noise. As the stars are not embedded within

the coma itself, the frames were kept with the stars present. It is evident that it would be more difficult to achieve a reliable solution for this small coma, which is not as symmetrical as that of 126P/IRAS, but the same process used for 126P/IRAS, was followed.

Fig. 20 displays all the simulations carried out overlaid on the 46P/Wirtanen data. Fig. 20a-l show simulations with values of α from 0.5 to 0.8, μ_g from 1 to 3. None produce a fit of the required quality to draw any conclusions about the comet properties. However, looking at the model outputs it is possible to discern how a better solution may be achieved by adjusting the simple inputs used. The fits of the best quality are those with high mass distribution indices $\alpha = 0.8$, so that the small grains dominate the surface area of the dust within the cometary coma. It is also clear that the slowest velocity used (i.e. with $\mu_g = 3$) produces fits that are closer to the observed data. All simulations produce isophotes that are much more widely spread than those observed in the comet and which extend beyond the head of the corresponding observed contours of the coma. 46P/Wirtanen is too faint to determine its outer apex boundary and even for the slowest velocities used the models' apexes were beyond the outer most observed contour in the comet. Therefore shown in Fig 20m-r are six additional simulations which demonstrate an improved quality of fit. With two different anisotropic source functions (0.75 +3.cos θ and 0.5+ 2 cos θ, SF1 and SF2 respectively) a dust to gas ratio of $\mu = 5.5$ and mass distribution index $\alpha = 0.7 - 0.9$

Table 4 lists the global χ^2 values of all the model outputs with the anisotropic source functions. The number of degrees of freedom (n) is 4900, i.e. much less than the 16900 for comet 126P/IRAS. If one wanted to compare the quality of the fits between the two comets the parameter χ^2/n can be used. The χ^2 parameter becomes very poorly behaved for these data; the noisy regions have a significant affect on the values calculated of up to approximately 200. Therefore of the six images shown, the best two were chosen by breaking the χ^2 down to look at individual contours and judgement by eye after discarding those with χ^2 values 200 more than the lowest value achieved of 1670.

The best two fits (Fig 20n and Fig 20q) both have a mass distribution index $\alpha = 0.8$ and a dust to gas ratio of 5.5. This translates to a velocity of approximately 2/3 of that seen in comet 126P/IRAS (i.e. for the 0.15 mm grains $V_T \sim 65$ m s^{-1}). Although the global χ^2 indicates that a better fit is achieved with the SF2 source function and $\alpha = 0.7$ a closer examination of the individual isophotes shows that this value is dominated by the outer, low quality contours.

The only difference between the two simulations is the input source function of the dust. Of these two final solutions, Fig. 20q with SF2 source function, is the more pleasing to the eye. It appears to represent the general shape of the coma quite well. However, the global χ^2 measurement indicates that Fig. 20n which use the SF1 source function has the better fit. As before χ^2 results for the individual contours were looked at in detail. This time however all measurements tended to support the global statistical result. The best solution therefore has the slightly weaker anisotropy. Comparing the luminosity of this image with the real data, and scaling the dust production rate accordingly, $Q_{dust} \sim 3$ kg s^{-1} is calculated. This therefore gives the following solution for comet 46P/Wirtanen:

- $\alpha = 0.8 \pm 0.15$ between 10^{-20} kg -10^{-4} kg
- The velocity of a 1 μm and 0.1 mm grain entering the outer coma is 35 m s^{-1} and 6.5 m s^{-1} respectively. Using equation (8) this is obtained with a dust to gas ratio $\mu_g = 5.5 \pm {}^{1}/_{3}$ and an active fraction $g = 0.03^{+0.15}/_{-0.01}$ assuming a 1 km radius nucleus, or with a $f = 0.01$ with equation (9).
- Dust production rate of $3\ ^{+7}/_{-1.5}$ kg s^{-1}
- A source function with a strong anisotropy towards the sun with a FWHM between 45^0 and 90^0 about the sun comet line.

The large errors on the dust to gas ratio reflect the fact that when μ_g gets this large its relative affect on the velocity reduces.

Colangeli *et al.* (1998) produced model fits to this comet from ISO data taken only 2 days

earlier. They calculated a dust production rate for the comet of 2 ± 1 kg s^{-1} for grains of 10 μm up to 0.1 cm in size which is in agreement with the value calculated here. They also came to the conclusion that the comet was emitting strongly towards the Sun. However, the mass distribution index of $\alpha \sim 0.5$ and velocities of ~ 20 m s^{-1} for mm sized particles are quite different to those seen within this work. There are two reasons that immediately spring to mind for these differences. Colangeli *et al.* (1998) concentrate on the large grains and do not consider grains smaller than 10 μm in size due to the wavelength at which the comet is being examined (large grains are better sampled in the IR than in the visible region of the spectrum). This can bias solutions towards the larger grains and obviously ignores micron-sized grains which can easily dominate the scattered light as shown in Fig 5. In simulations carried out by Fulle the value of Q_{pr} is always 1, applicable to the larger grains.

Rickman and Jorda (1998) report an apparently entirely active surface. However, this is based on data near perihelion and they infer that this is either a consequence of the model being used or fragmentation of surface layers near perihelion. The active fraction, *g*, that we derive for Wirtanen, is a secondary parameter produced from constraining the dust velocity within the coma model presented and thus should not be taken as an absolute measure. An alternative solution can be obtained by reducing the dust to gas ratio to 2 and increasing the active fraction to $g = 0.1$ using equation (8). This demonstrates the limitation of dust coma modelling when applied only to individual images; it can be used to constrain the velocity of grains but not necessary secondary parameters such as the dust to gas ratio and active fraction. These values can be derived if other data are available, such as gas production rate observations (Bertaux *et al* 1999), which would directly constrain the dust to gas ratio. It should be noted that a more recent estimate of the icy fraction *f* of up to 15%, has been made by Groussin and Lamy (2003), which is more consistent with our work. If the active fraction (g) were increased to 100 % as measured by Rickman and Jorda the dust to gas ratio would have to be $<< 1$.

5 CONCLUSIONS

A new cometary coma model has been presented, characterised, tested and applied to ground based photometric observations of two comets. The main conclusions drawn from the model's performance are presented below, together with an assessment of the model's ability to constrain the physical properties of a comet's dust coma.

1. The mass distribution index can only be poorly constrained by dust coma models. This is particularly true when alpha is < 0.66, when the surface area of dust in the coma is dominated by the large grains. The derived uncertainty for the mass distribution index is ± 0.15 for $\alpha > 0.66$ and ± 0.2 for $\alpha < 0.66$. The result is demonstrated if the grain trajectories are calculated with either the full orbital dynamics or with a standard fountain model. This distinct lack of variation for a low mass distribution in the model output is caused by the lower spatial dispersion of grains larger than 50 μm in size throughout the coma for a given time increment. The estimated uncertainty in α is therefore higher than that given by previous authors.
2. The scattering of light does not display a simple relationship with grain size. Therefore grains over the whole size range must be used with an appropriate scattering law to fully reproduce a cometary coma observation. It is important to quote the particle mass limits used when determining mass production rates. Observations at different wavelengths are more sensitive to different particle size ranges. Scattering is dependent on the total scattering area and scattering efficiency, which is larger for grains of similar size to the wavelength (sub-micron for scattering at visible wavelengths). Thermal IR emission is more efficient for distinguishing the contribution from larger grains, particularly if spectral information is available. The observations are however more difficult to make, particularly for fainter

comets.

3. The model displays sensitivity to the velocity at which the grains enter the collisionless region. With other physical parameters known, the mean velocity of the dust grains entering the outer coma can be well constrained, within a few m s^{-1} for the grains with a radius of 0.1 mm. This implies that the velocities predicted by inner coma models for a given comet can be tested with a degree of confidence. However secondary parameters such as dust to gas ratio, which can be inferred from the dust grain velocity, should not be derived as an absolute measure using this technique.
4. Jets or dust concentrations emitted from the inner coma can be simulated in the model. Since artefacts that look like jets can be produced by other inputs, strong observational evidence would be required independently, that concentration of activity exists at the edge of the inner coma for a particular comet, before they could be introduced confidently into a simulation. This is also true of rotation of the comet, which can be modelled about any axis to a large degree of complexity.
5. Although individual jets can be observed at a level of a few percent above the background coma intensity in the line of sight column integrated images, the local dust density enhancement in a jet must be much greater than this. Without a series of observations to identify the evolution of such jets, it is not possible to constrain jets from the shape of the outer coma unless it has a much greater dust density than the surrounding environment (> a factor of 1000). Additionally, multiple jets (with densities < 1000 times that of the surrounding environment) within the inner coma form a uniform outer coma and thus cannot be clearly identified from a single ground based observation.
6. The expected anisotropy in activity towards the Sun can be estimated by the model very approximately. Additional observational evidence would be required to provide an estimate better than a cone of ± 30 degrees.
7. Modelling the pseudo surface as an ellipsoid produces artefacts very similar to those introduced by modelling jets in the comet's coma. This immediately demonstrates how the uniqueness of the solution may be diminished as two separate nucleus properties give very similar model outputs. This result does not reveal what affect an ellipsoidal nucleus has on the final shape of a comet coma but rather the affect of having the dust emitted on vectors dictated by the nucleus shape. This also shows that although the model can constrain parameters such as the size distribution of dust production, additional data at different wavelengths from the ground and in-situ measurements are required to fully characterise a given comet.
8. Recent results from the Stardust mission have demonstrated the importance of fragmentation in a cometary coma (Green *et al.* 2004). Although fragmentation is clearly an important process, it occurs mostly on scales much smaller than that observed in ground based images. The bursts of particles impacting Stardust have been interpreted as localized clouds of fragmented particles a few hundred metres (or smaller) up to a few km in dimension. As they expand, they gradually disperse into the coma. The resolution of ground based images is such that either many clouds will be seen in a given pixel, or the clouds will have dispersed into the background. Therefore the effects of fragmentation on the scattering are effectively already taken into account by this model. However, if a significant amount of fragmentation occurs outside the inner coma, then the velocity dispersion of grains will be affected since small grains will, initially, have speeds corresponding to those of their larger parents.
9. Using the full orbital dynamics to calculate the dust trajectories does significantly affect the coma shape, especially if large dust grains dominate the coma.
10. The model has been successfully applied to two comets 126P/IRAS and 46P/Wirtanen. The model has demonstrated an ability to loosely constrain a number of these comets' physical properties including the mass distribution index and the dust production rate. The calculated

dust production rate for comet 46P/Wirtanen is in good agreement with ISO observations made by Colangeli *et al.* (1998) at ~ 3 kg s^{-1} while comet 126P/IRAS displays a much higher rate of ~50 kg s^{-1}. The mean mass distribution index is 0.8 in both although the velocity of the dust grains varies by a bout 50 % between the two cases : 55 ms^{-1} for a 1 μm in comet 126P/IRAS and 35 ms^{-1} for a 1 μm in 46P/Wirtanen.

Acknowledgements
This paper uses observations made at the South African Astronomical Observatory (SAAO), we thank the SAAO staff for their assistance during our visit. The observations were taken as part of a Rosetta/ISO target comet programme with A. Rotundi (Istituto Universitario Navale, Napoli). S. Green and N. McBride acknowledge the financial support of the UK Particle Physics and Astronomy Research Council. M. Foster is indebted to Lidar Technologies, Ltd for making time available for this project.

REFERENCES

A'Hearn M.F., Belton M.J.S., Delamere W.A., Kissel J., Klaasen K.P., McFadden L.A., Meech K.J., Melosh H.J., Schultz P.H., Sunshine J.M., Thomas P.C., Veverka J., Yeomans D.K., Baca M.W., Busko I., Crockett C.J., Collins S.M., Desnoyer M., Eberhardy C.A., Ernst C.M., Farnham T.L., Feaga L., Groussin O., Hampton D., Ipatov S.I., Li J.-Y., Lindler D., Lisse C.M., Mastrodemos N., Owen W.M., Richardson J.E., Wellnitz D.D., White R.L., 2005, Sci, 310, 258.

Belton J.S., Mueller B.E.A., Julian W.H., Anderson A.J., 1991, Icarus, 93, 183.

Bertaux J.L., Costa. J., Makinen. T., Qeumerias. E., Lallement. R., Kyrola. E., Schmidt. W., 1999 Planet, Space. Sci. 47, 725

Britt D.T., Boice D.C., Buratti B.J., Campins H., Nelson R.M., Oberst J., Sandel B.R., Stern S.A., Soderblom L.A., Thomas N., 2004, Icarus, 167, 45.

Brownlee D.E., 1978, in Cosmic Dust, McDonnell J.A.M., ed, Wiley, New York, p295.

Brownlee D.E., Horz F., Newburn R.L., Zolensky M., Duxbury T.C., Sandford S., Sekanina Z., Tsou P., Hanner M.S., Clark B.C., Green S.F., Kissel J., 2004, Sci, 304, 1764.

Clark B.C., Green S.F., Economou T.E., Sandford S.A., Zolensky M.E. Brownlee D.E., 2004, J. Geophys. Res., 109 E12S03.

Colangeli L., Bussoletti E., Pestellini C.C., Fulle M., Mennella V., Palumbo M., Rotundi A., 1998, Icarus, 134, 35.

Crifo J.F., 1994, Current Science, 66, 583.

Crifo J., 1995, ApJ, 445, 470.

Crifo J.F., Rodionov A.V., 1997, Icarus, 127, 319.

Crifo J.F., Rodionov A.V., 1999, in Asteroids, Comets Meteors, Cornell 1999, Abstracts Volume,

p34.

Delsemme A.H., Miller D.C., 1971, Planet. Space Sci., 19, 1229.

Divine N., 1981, in The Comet Halley Dust and Gas Environment, ESA SP-174, p25.

Divine N., Fechtig H., Gombosi T.I., Hanner M.S., Keller H.U., Larson S.M., Mendis D.A., Newburn R., Rienard R., Sekanina Z., Yeomans D.K., 1986, Space Sci. Rev., 43, 1.

Draine B.T., 1985, ApJ Suppl., 57, 587.

Duxbury T.C., Newburn R.L., Brownlee D.E., 2004, J. Geophys. Res, 109, E12S02.

Eaton N., 1984, Vistas in Astronomy, 27, 111.

Eddington A.S., 1910, MNRAS, 70 442-458.

Edenhofer P., Bird M.K., Brenkle J.P., Buschert H., Kursinski E.R., Motinger N.A., Porsche H., Stelzreid C.T., Volland H., 1987, A&A, 187, 712.

Epifani E., Rotundi A., Foster M.J., Green S.F., Colangeli L., Fulle M., Menella V. Palumbo P. 1999, Planet. Space Sci., 47, 765.

ESA, 1993, Rosetta Comet Rendezvous Mission, ESA SCI (93)7.

Fertig J., Schwehm G. H., 1984, Adv. Space. Res., 9, 213.

Finson M.L., Probstein R.F., 1968a, ApJ, 154, 327.

Finson M.L., Probstein R.F., 1968b, ApJ, 154, 353.

Fulle M., 1987, A&A, 171, 327.

Fulle M., 1989, A&A, 217, 283.

Fulle M., 1996, A&A, 311, 333.

Fulle M., Levasseur-Regourd A.C., McBride N., Hadamcik E., 2000, AJ, 119, 1968.

Gombosi T.I., Nagy A.F., Cravens T.E., 1986, Reviews of Geophysics, 24, 667.

Green S.F., McDonnell J.A.M., McBride N., Colwell M.T.S.H., Tuzzolino A.J., Economou T.E., Tsou P., Clark B.C., Brownlee D.E., 2004, J. Geophys. Res, 109, E12S04.

Groussin O., Lamy P., 2003, A&A, 412, 879.

Gustafson B.A.S.,1989, ApJ, 337, 945.

Gustafson B.A.S., Kolokolova L., Waldermasson Y.U., Xu Y.L., 1999, in Asteroids, Comets Meteors, Cornell 1999, Abstracts Volume, p88.

Hanner M.S., 1983, Conference on cometary exploration, Budapest 1982, p1.

Jessberger E.K., Christoforidis A., Kissel J., 1988, Nature, 332, 691.

Jewitt D., 1991, in Newburn R.L., Neugebauer, M., Rahe, J., eds, Comets in the Post Halley Era, p19.

Jorda L. Gutiérrez, P., 2002, Earth, Moon & Planets, 89, 135.

Kattawar G. W., Plass G. N., 1967, Appl. Opt., 6, 1377.

Keller H.U., Arpigny C., Barbieri C., Bonnet R.M., Cazes S., Coradini M., Cosmovici C.B., Delamere W.A., Huebner W.F., Hughes D.W., Jamar C., Malaise D., Reitsema H.J., Schmidt H.U., Schmidt W.K.H., Seige P., Whipple F.L., Wilhelm K., 1986, Nat, 321, 320.

Keller H.U., Delamere W.A., Reitsema H.J., Huebner W.F., Schmidt H.U., 1987, A&A, 187, 807.

Keller H.U., Kramm R., Thomas N., 1988, Nat, 331, 227.

Keller H.U., 1990, in Mason J.W., ed, Comet Halley: Investigations, Results, Interpretations. Vol. 2: Dust, Nucleus, Evolution, Ellis Horwood/Prentice-Hall, Chichester, p133.

Kissel J., Brownlee D.E., Buchler K., Clark B.C., Fechtig H., Grün E., Hornung K., Igenbergs E.B., Jessberger E.K., Krueger F.R., Kuczera H., McDonnell J.A.M., Morfill G.M., Rahe J., Schwehm G.H., Sekanina Z., Utterback N.G., Volk H.J., Zook H.A., 1986a, Nat, 321, 336.

Kissel J., Sagdeev R.Z., Bertaux J.L., Angarov V.N., Audouze J., Blamont J.E., Buchler K., Evlanov E.N., Fechtig H., Fomenkova M.N., von Hoerner H., Inogamov N.A., Khromov V.N., Knabe W., Krueger F.R., Langevin Y., Leonasv B., Levasseur-Regourd A.C., Managadze G.G., Podkolzin S.N., Shapiro V.D., Tabaldyev S.R., Zubkov B.V., 1986b, Nat, 321, 280.

Kissel J., Krueger F.R., 1987, Nat, 326, 755.

Lisse C.M., A'Hearn M.F., Fernandez Y., Lien D., Peschke S., 1999, in Asteroids, Comets Meteors, Cornell 1999, Abstracts Volume, p85.

Massone L., 1987, PhD Thesis, Ruprecht-kurls Universitat Hiedelberg, Germany

Mazets E.P., Aptekar R.L., Golenetskii S.V., Guryan Yu.A., Dyachkov A.V., Ilyinskii V.N., Panov V.N., Petrov G.G., Savvin A.V., Sagdeev R.Z., Sokolov I.A., Khavenson N.G., Shapiro V.D., Shevchenko V.I., 1986, Nat, 321, 276.

Mazets E.P., Sagdeev R.Z., Aptekar R.L., Golenetskii S.V., Guryan Y.A., Dyachkov A.V., Ilyinskii V.N., Panov V.N., Petrov G.G., Savvin A.V., Sokolov I.A., Frederiks D.D., Khavenson N.G., Shapiro V.D., Shevchenko V.I., 1987, A&A, 187, 699.

McBride N., Green S.F., Levasseur-Regourd A.C., Goidet-Devel B., Renard J., 1997, MNRAS, 289, 535.

McDonnell J.A.M., Alexander W.M., Burton W.M., Bussoletti E., Evans G.C., Evans S.T., Firth J.G., Grard R.J.L., Green S.F., Grün E., Hanner M.S., Hughes D.W., Igenburgs E., Kissel J.,

Kuczera H., Lindblad B.A., Langevin Y., Mandeville J.C., Nappo S., Pankiewicz G.S.A., Perry C.H., Schwehm G.H., Sekanina Z., Stevenson T.J., Turner R.F., Weishaupt U., Wallis M.K., Zarnecki J.C., 1987, A&A, 187, 719.

McDonnell J.A.M., Lamy P.L., Pankiewicz G.P., 1991, in Newburn R.L., Neugebauer M., Rahe J., eds, Comets in the Post-Halley Era Vol. 2, Kluwer, Dordrecht, p1043.

McDonnell J.A.M., McBride N., Beard R., Bussoletti E., Colangeli L., Eberhardt P., Firth J.G., Grard R., Green S.F., Greenberg J.M., Grün E., Hughes D.W., Keller H.U., Kissel J., Lindblad B.A., Mandeville J.C., Perry C.H., Rembor K., Rickman H., Schwehm G.H., Turner R.F., Wallis M.K., Zarnecki J.C., 1993, Nat, 362 ,732.

Meech K.J., Bauer J.M., Hainaut O.R., 1997, A&A, 326, 1268.

Mukai T., 1989, in Bonetti A., Greenberg J.M., Aiello S., eds, Evolution of Interstellar Dust and Related Topics, Elsevier, New York, p397.

Nelson R.M., Soderblom L.A., Hapke B.W., 2004, Icarus, 167, 37.

Oberst J., Giese B., Howington-Kraus E., Kirk R., Soderblom L., Buratti B., Hicks M., Nelson R., Britt D., 2004, Icarus, 167, 70.

Perry C.H., Green S.F., McDonnell J.A.M., 1987, NASA Conference Publication 3004 178-179

Purcell E.M., Pennypacker C.R., 1973, ApJ, 186, 705.

Probstein R.F., 1969, in Problem of Hydrodyanmics and the Continuum Mechanics, Lavert'ev M.A., ed, Philadelphia p568.

Rickman H., Jorda, L., 1998, Adv. Space Res.11, 1491.

Rodionov A.V., Jorda L., Jones G.H., Crifo J.F., Colas F., Lecacheux J., 1999, Icarus, 136, 232.

Sagdeev R.Z., Szabo F., Avanesov G.A., Cruvellier P., Szabo L., Szego K., Abergel A., Balazs A., Barinov I.V., Bertaux J.-L., Blamount J., Detaille M., Demarelis E., Dul'Nev G.N., Endroczy G., Gardos M., Kanyo M., Kostenko V.I., Krasikov V.A., Nguyen-Trong T., Nyitrai Z., Reny I., Rusznyak P., Shamis V.A., Smith B., Sukhanov K.G., Szabo F., Szalai S., 1986, Nat, 321, 262.

Sagdeev R.Z., Szegö K., 1990, in Mason J.W., ed, Comet Halley: Investigations, Results, Interpretations, Vol. 2: Dust, Nucleus, Evolution, Ellis Horwood/Prentice-Hall, Chichester, p147.

Schleicher D.G., Woodney L.M., 2003, Icarus, 162, 190.

Sekanina Z., 1974, in 'The study of comets', NASA conference at the Goddard Space Flight Centre, p893.

Sekanina Z., 1979, in Longdon N., ed, The Comet Halley Micro-meteoroid Hazard, ESA SP-153, p25.

Sekanina Z., 1986, Adv. Space. Res., 5, 307.

Sekanina Z., Brownlee D.E., Economou T.E., Tuzzolino A.J., Green S.F., 2004, Sci, 304, 1769.

Simpson J.A., Sagdeev R.Z., Tuzzolino A.J., Perkins M.A., Ksanfomality L.V., Rabinowitz D., Lentz G.A., Afonin V.V., Ero J., Keppler E., Kosorokov J., Petrova E., Szabo L., Umlauft G., 1986, Nat, 321, 278.

Simpson J.A., Rabinowitz D., Tuzzolino A.J., Ksanfomality L.V. Sagdeev R.Z., 1987, A&A, 187, 742.

Simpson J.A., Tuzzolino A.J., Ksanfomality L.V., Sagdeev R.Z., Vaisberg O.L., 1989, Adv. Sp. Res., 9, 259.

Soderblom L.A., Boice D.C., Britt D.T., Brown R.H., Buratti B.J., Kirk R.L., Lee M., Nelson R.M., Oberst J., Sandel B.R., Stern S.A., Thomas N., Yelle R.V., 2004, Icarus, 167, 4.

Thomas N., Keller H.U., 1987, A&A, 187, 843.

Tuzzolino A.J., Economou T.E., Clark B.C., Tsou P., Brownlee D.E., Green S.F., McDonnell J.A.M., McBride N., Colwell M.T.S.H., 2004, Sci, 304, 1776.

van de Hulst H.C., 1957, Light scattering of small particles, John Wiley New York Academic Press.

Vaisberg O.L., Smirnov V.N., Gorn L.S., Iovlev M.V., Balikchin M.A., Klimov S.I., Savin S.P., Shapiro V.D., Shevchenko V.I., 1986, Nat, 321, 274.

Vaisberg O.L., Smirnov V., Omel'Chenko A., Gorn L., Iovlev M., 1987, A&A, 187, 753.

Vaisberg, O.L., 1990, Mason, J.W., ed, Comet Halley: Investigations, Results, Interpretations. Vol. 2: Dust, Nucleus, Evolution, Ellis Horwood/Prentice-Hall, Chichester, p.33.

Wallis M.K., 1982, in Wilkening, L., ed, Comets, University of Arizona Press p357.

Whipple F.S., 1951, ApJ, 118, 464.

Whipple F.L., 1982, in Wilkening, L., ed, Comets, University of Arizona press. p227.

Table 1: Comets encountered by spacecraft

Comet	Mission	Date	Distance (km)	Relevant observations
21P/Giacobini-Zinner	ICE	11/09/85	~8 000	Re-targeted magnetospheric explorer. No imaging or nucleus data.
1P/Halley	Vega 1	6/3/86	8 890	Nucleus properties [1-4]
	Vega 2	9/3/86	8 030	Dust spatial and mass distribution (10^{-18}-10^{-5} kg) [5-15]
	(Suisei)	8/3/86	151 000	Dust coma structure [16,17]
	(Sakigake)	11/3/86	7×10^6	Silicate and organic dust grains [18-22].
	Giotto	14/3/86	600	
26P/Grigg-Skjellerup	Giotto	10/7/92	~100	Dust mass distribution (10^{-9}–10^{-5} kg) [23]
				Dust coma structure [24]
19P/Borrelly	Deep Space 1	22/9/01	2 200	Nucleus properties and coma structure [24-27]
81P/Wild 2	Stardust	4/1/04	236	Nucleus properties [28,29]
				Dust spatial and mass distribution (10^{-14}-10^{-6} kg) [30,31]
				Dust coma structure [32,33]
9P/Tempel 1	Deep Impact	4/7/05	500 0!	Nucleus properties [33].

References: [1-4] Keller, 1990; Keller *et al.,* 1986; Keller, Kramm & Thomas, 1988; Sagdeev *et al.,* (1986); [5-15] Edenhofer *et al.,* 1987; Mazets *et al.,* 1986, 1987; McDonnell *et al.,* 1987; McDonnell, Lamy & Pankiewicz, 1991; Simpson *et al.,* 1986, 1987, 1989; Vaisberg, 1990; Vaisberg *et al.,* 1986, 1987; [16] Sagdeev and Szegö, 1990; Thomas & Keller, 1987; [18-22] Jessberger, Christoforidis & Kissel, 1988; Kissel *et al.*, 1986a, 1986b, Kissel & Krueger, 1987; [23] McDonnell *et al.,* 1993; [24] McBride *et al.,* 1997; [24-27] Britt *et al.,* 2004; Nelson *et al.,* 2004; Oberst *et al.*, 2004; Soderblom *et al.,* 2004; [28,29] Brownlee *et al.,* 2004; Duxbury, Newburn & Brownlee, 2004; [30,31] Tuzzolino *et al.,* 2004; Green *et al.,* 2004; [32] Sekanina *et al.,* 2004; [33] A'Hearn *et al.,* 2005.

Table 2: Comets 46P/Wirtanen and 126P/IRAS at time of observations

Object	Date	Heliocentric distance r_h (AU)	Geocentric Distance Δ (AU)	Phase Angle α_1 °
46P/Wirtanen	10/11/96	1.850	1.677	32.1
	11/11/96	1.842	1.68	32.2
126P/IRAS	10/11/96	1.706	1.287	35.2
	11/11/96	1.707	1.298	35.2

Table 3: χ^2 values for model fits applied to comet 126P/IRAS

	Mass distribution Index (α)	**Dust to gas ratio (μ)**	χ^2
a	0.5	1	5358
b	"	2	5391
c	"	3	7393
d	0.6	1	5198
e	"	2	4853
f	"	3	6674
g	0.7	1	4906
h	"	2	4281
i	"	3	6001
j	0.8	1	4096
k	"	2	3989
l	"	3	6149
m	"	1.5	3702
n	0.9	2	4784

Table 4: χ^2 values for model fits applied to comet 46P/Wirtanen

Mass Distribution Index α	**Emission function SF1** **0.75 + 3.6 Cos 2θ**	**Emission function SF2** **0.5 + 2Cos 2θ**
0.9	1973	1955
0.8	1794	1670
0.7	1784	2796

Figure captions

Fig. 1 The geometry system of the cometary coma model. (A) Dust emission from the cometary nucleus. (B) The relative positions of the Sun, Earth and Comet and the orientation of the cometocentric reference frame.

Fig. 2 Flow chart describing the cometary coma model.

Fig. 3 The size dependent velocity function: Open squares and open triangles calculated with equation (9) with $f(r)$ = 0.01, and $f(r)$ = 0.03 respectively; filled large circles and filled small circles calculated with equation (8) with μ= 1 and 3 respectively.

Fig. 4 The radiation pressure efficiency factor as a function of grain radius for amorphous carbon (crosses - refractive index 1.92 + 0.77i) and silicate grains (circles – refractive index 1.6 + 0.5i).

Fig. 5 Total number of photons scattered towards the Earth (per m^2)from a comet with a heliocentric distance of 0.94 AU and a geocentric distance of 0.34 AU as a function of mass distribution index.

Fig. 6 Total number of photons scattered towards the Earth (per m^2) from a comet with a heliocentric distance of 0.94 AU and a geocentric distance of 0.34 AU as a function of grain size for values of α from 0.4 – 0.8.

Fig. 7 Synthetic images produced using the nominal model with the mass distribution index α varied from 0.8 – 0.5 for both the fountain model (a-c) and full orbital dynamics (d-f); X is the Sun comet axis, Z is the Earth comet axis, and Y is the perpendicular to this plane. The pixel size is 1000 km and the image covers 200 000 x 200 000 km.
a) Fountain model α=0.4 b) Fountain model α=0.6 c) Fountain model α=0.8
d) Orbital dynamics α=0.4 e) Orbital dynamics l α=0.6 f) orbital dynamics α=0.8

Fig. 8 The relative change of the model output shape as a function of changing mass distribution index, expressed as a χ^2 for both the fountain (open circles) and full orbital (filled circles) dynamic models

Fig. 9 Synthetic images produced using the nominal model with the velocity calculated by equation (8): Grain speeds are varied by adjusting the dust to gas ratio from μ=1-3 for both the fountain model (a-c) and full orbital dynamics (d-f); Geometry as in Fig. 7.
a) Fountain model μ=1 b) Fountain model μ=2 c) Fountain model μ=3
d) Orbital dynamics μ=1 e) Orbital dynamics μ=2 f) Orbital dynamics μ=3

Fig. 10 The relative change of the model output shape as a function of varying velocity using the dust to gas ratio in equation (8), expressed as a χ^2 for both the fountain (open circles) and full orbital (filled circles) dynamic models

Fig. 11 Synthetic images produced using the nominal model with the velocity calculated by equation (9). Grain speed are varied by adjusting the icy fraction from $f(r)$ =0.01 - 0.05; Geometry as in Fig. 7.
a) Eq (9), f = 0.01 b) Eq (9), f = 0.03 c) Eq (9), f = 0.05

Fig. 12 The relative change of the model output shape as a function of varying velocity using the active icy fraction term in equation (9), expressed as a χ^2.

Fig. 13 Synthetic images produced using the nominal model with different activity functions: (a) $\cos^2\theta$ in the sunward direction (b) $\cos^2\theta/2$ sunward bias and (c) $5+3\cos\theta$ sunward bias; Geometry as in Fig. 7.

Fig. 14 Synthetic images produced using the nominal model with a uniform activity function with a jet simulated from a single location on the nucleus surface: (a) jet emits 100 more dust than surrounding area, (b) jet emits 1000 more dust than surrounding area and (c) jet emits 10000 more dust than surrounding area; Geometry as in Fig. 7.

Fig. 15 Synthetic images produced by an ellipsoid with nominal model properties. In each case, one axis is twice the size of the other two: (a) with elongation aligned with the sun comet direction (b) elongation along perpendicular to the plane of the page, (c) elongation in the plane of the page and perpendicular to the Sun-comet direction; Geometry as in Fig. 7.

Fig. 16 Synthetic images produced using the nominal model comet rotated: (a) comet is isotropically emitting rotated about the x axis, (b) a comet displaying a sunward bias activity function rotated about the z axis and (c) a comet with a sunward bias activity function rotated about the y axis; Geometry as in Fig. 7.

Fig. 17 Contour map of Comet 126P/IRAS. Pixel size = 0.35 arcseconds. Contour levels staring from the centre in magnitudes per pixel are 20.98, 21.58, 22.18, 22.78, 23.38, 23.98, 24.58. The arrow marks the direction to the Sun, the pixel size is 429 km and the image covers 60 000 x 60 000 km.

Fig. 18 Model contour maps for comet 126P/IRAS overlaid on real image for $\alpha =$ 0.5-0.9 (top to bottom) and $\mu =$ 1-3 (left to right) with an isotropic emission function.

a) $\alpha = 0.5, \mu = 1$ b) $\alpha = 0.5, \mu = 2$ c) $\alpha = 0.5, \mu = 3$
d) $\alpha = 0.6, \mu = 1$ e) $\alpha = 0.6, \mu = 2$ f) $\alpha = 0.6, \mu = 3$
g) $\alpha = 0.7, \mu = 1$ h) $\alpha = 0.7, \mu = 2$ i) $\alpha = 0.7, \mu = 3$
j) $\alpha = 0.8, \mu = 1$ k) $\alpha = 0.8\ \mu = 2$ l) $\alpha = 0.8, \mu = 3$
m) $\alpha = 0.8, \mu = 1.5$ n) $\alpha = 0.9, \mu = 2$

Fig. 19 Contour map of Comet 46P/Wirtanen . Pixel size = 0.35 arcseconds. Contour levels starting from the centre in magnitudes per pixel are 23.29, 23.89, 24.48, 25.09, 25.69. The arrow marks the direction to the Sun, the pixel size is 1276 km (after binning) and the image covers 90 000 x 90 000 km.

Fig. 20 Model contour maps for comet 46P/Wirtanen overlaid on the real image for a range of mass distribution indices, α, dust to gas ratios, μ,, and activity functions (see text for details).
SF = Source function, (I if the source used is isotropic).

a) $\alpha = 0.5, \mu = 1$, SF=I b) $\alpha = 0.5, \mu = 2$, SF=I c) $\alpha = 0.5, \mu = 3$, SF=I
d) $\alpha = 0.6, \mu = 1$ SF=I e) $\alpha = 0.6, \mu = 2$ SF=I f) $\alpha = 0.6, \mu = 3$ SF=I
g) $\alpha = 0.7, \mu = 1$, SF=I h) $\alpha = 0.7, \mu = 2$, SF=I i) $\alpha = 0.7, \mu = 3$, SF=I
j) $\alpha = 0.8, \mu = 1$, SF=1 k) $\alpha = 0.8, \mu = 2$, SF=I l) $\alpha = 0.8, \mu = 3$ SF=I
m) $\alpha = 0.7, \mu = 5.5$, SF= $0.75 + 3\cos\theta$
n) $\alpha = 0.8, \mu = 5.5$, SF= $0.75 + 3\cos\theta$
o) $\alpha = 0.9, \mu = 5.5$, SF= $0.75 + 3\cos\theta$

p) α=0.7, μ= 5.5, SF= 0.5 + 2 cos θ
q) α=0.8, μ= 5.5, SF= 0.5 + 2 cos θ
r) α=0.9, μ= 5.5, SF= 0.5 + 2 cos θ

Foster and Green Fig. 1

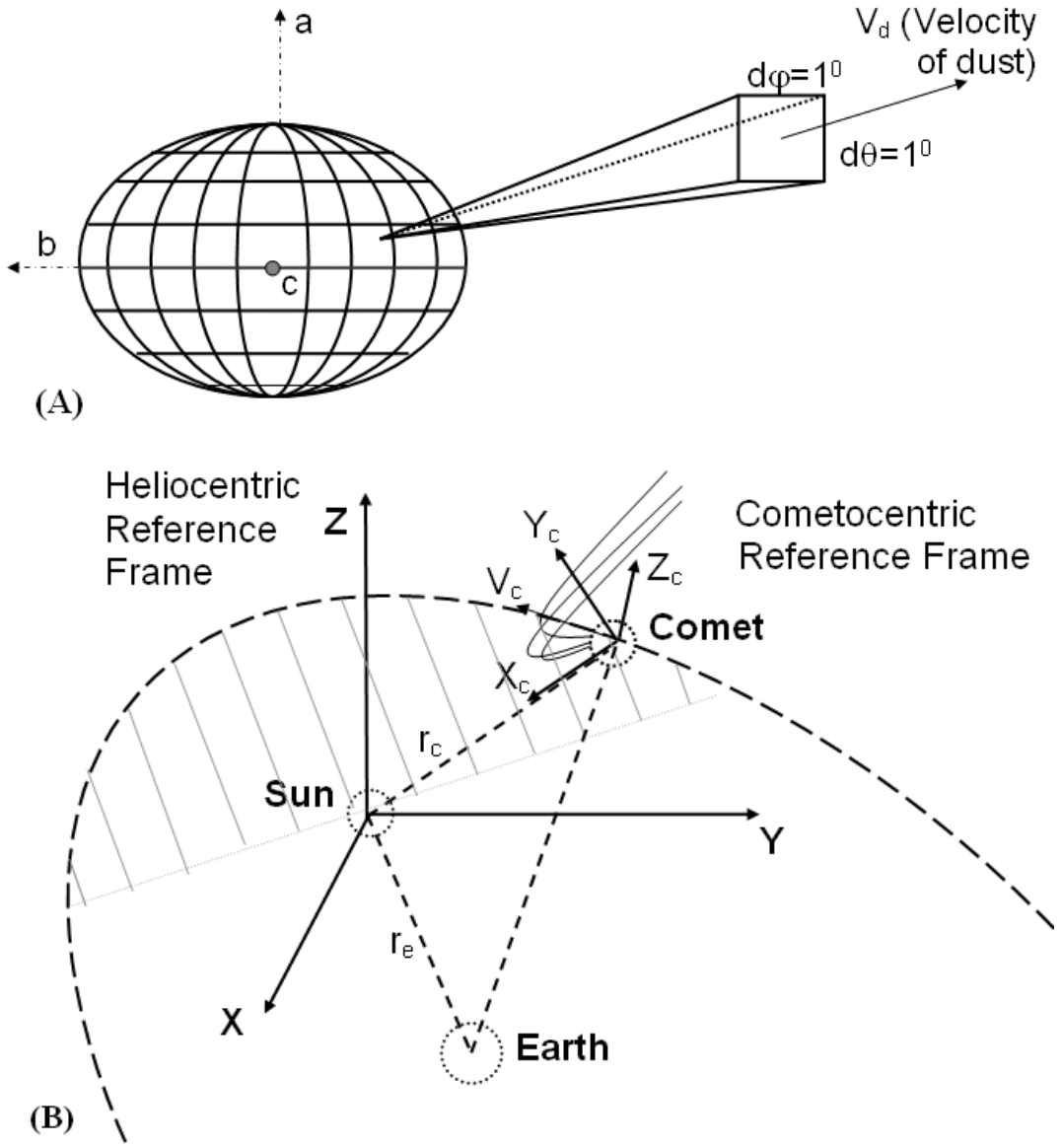

Foster and Green Fig 2

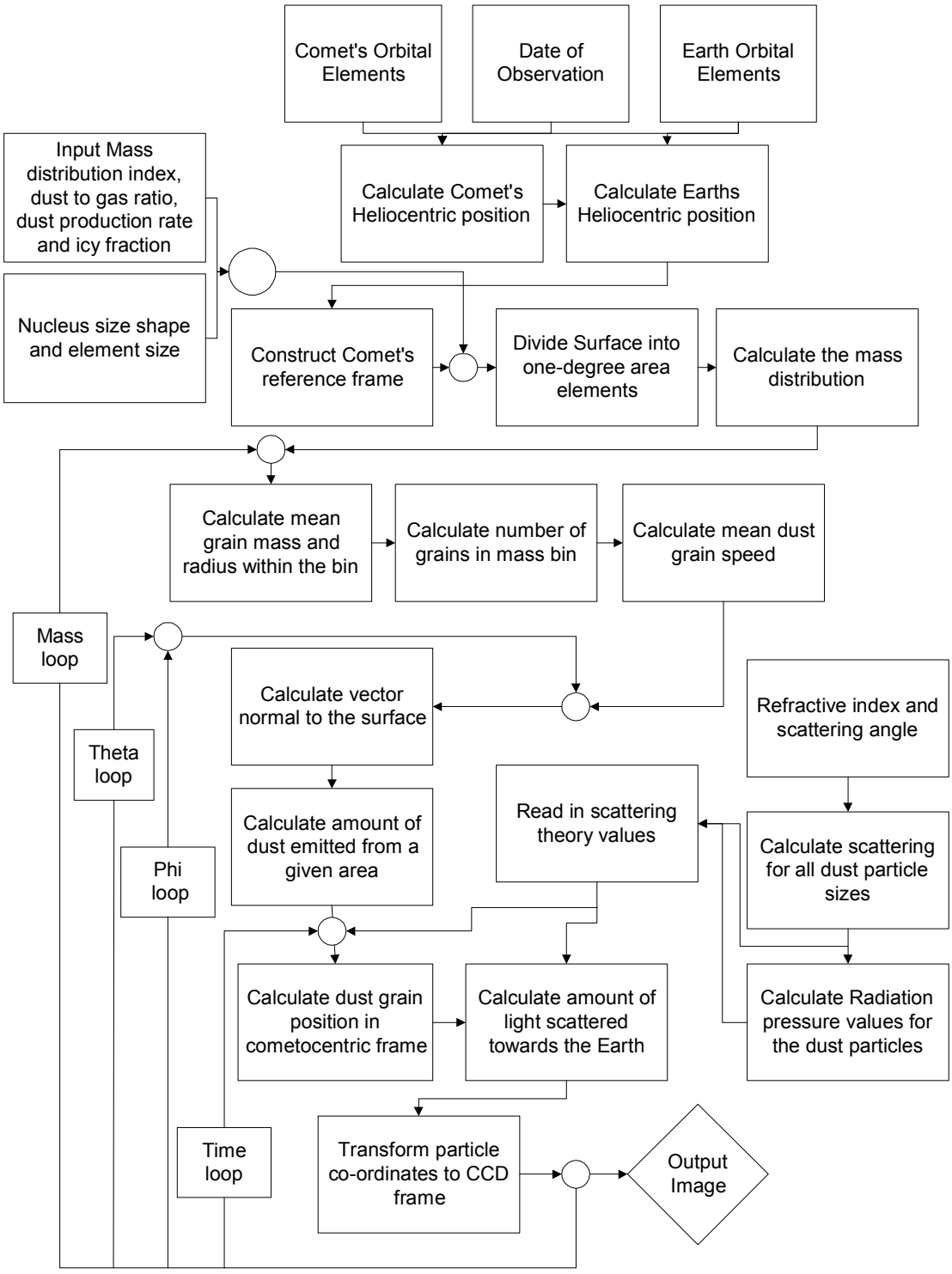

Foster and Green Fig 3

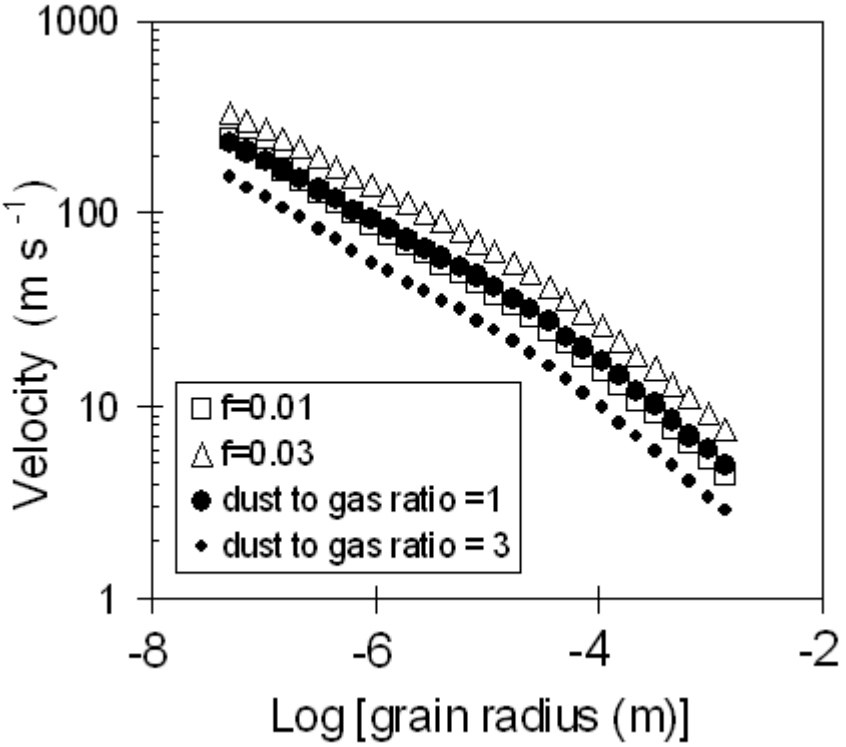

Foster and Green Fig 4

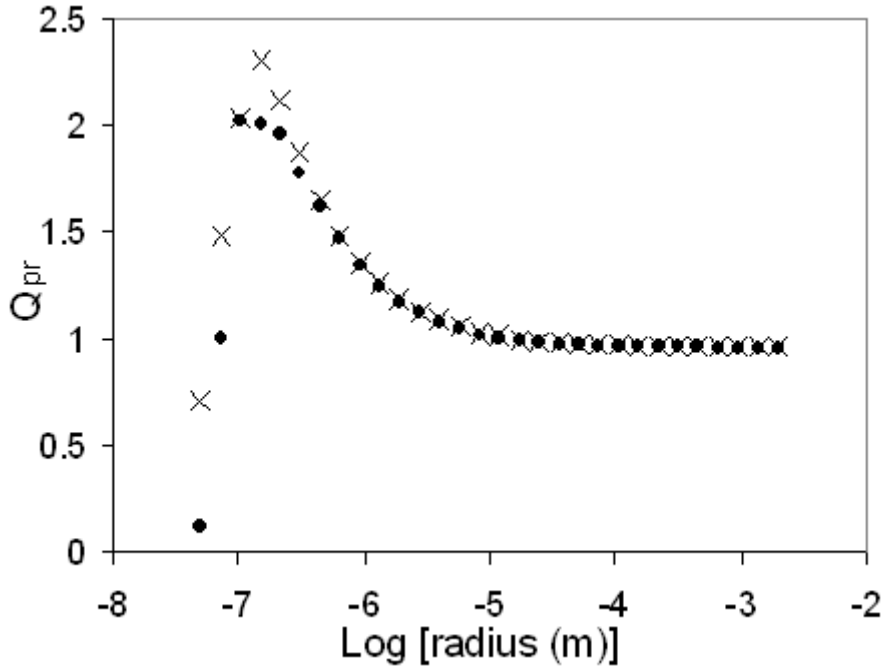

Foster and Green Fig 5

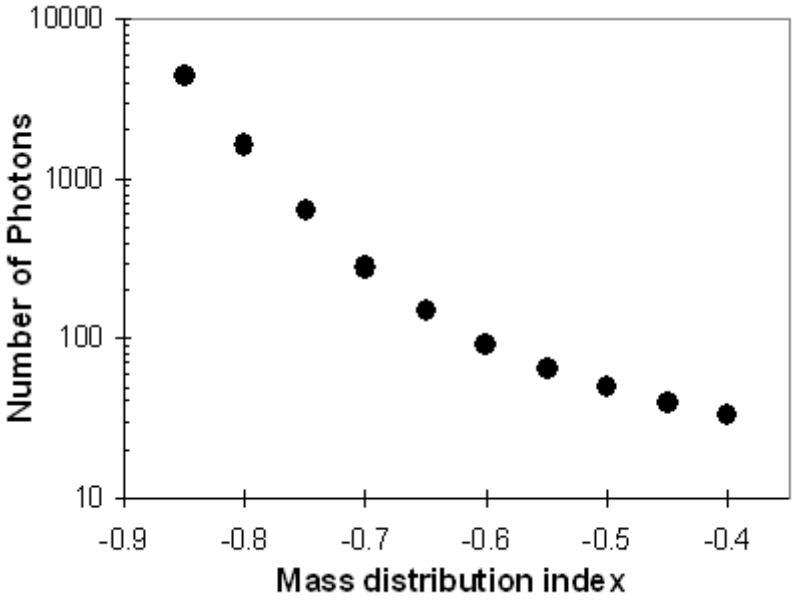

Foster and Green Figure 6

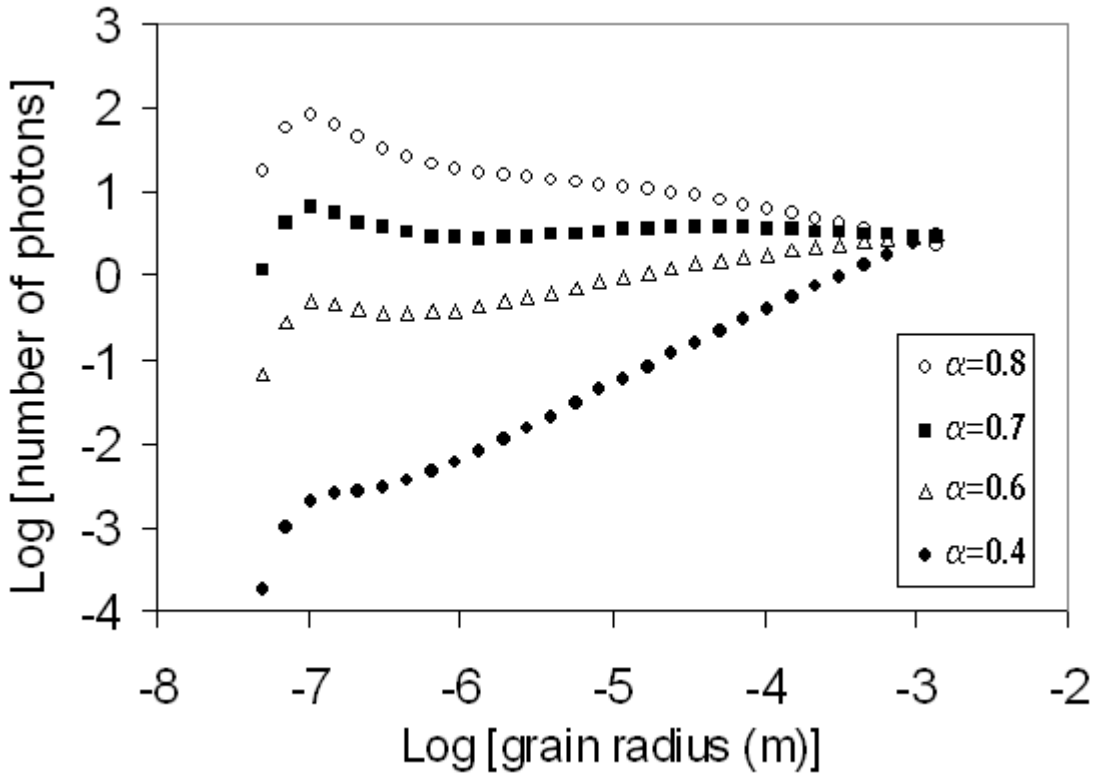

Foster and Green Fig 7

a) Fountain model α=0.4 b) Fountain model α=0.6 c) Fountain model α=0.8

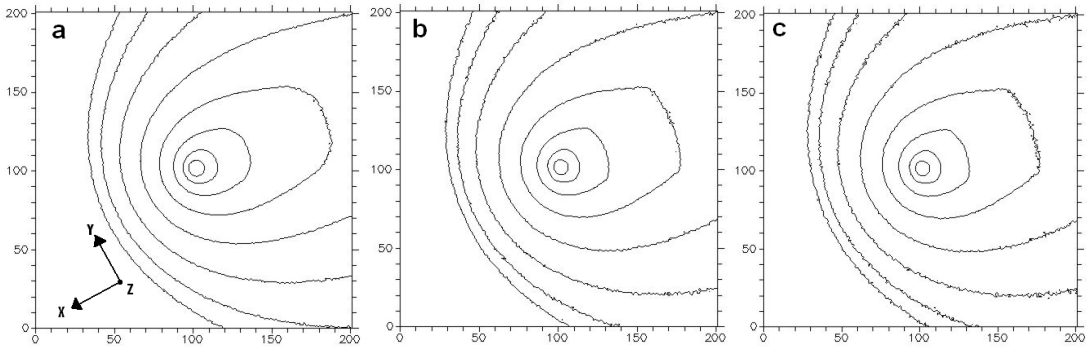

d) Orbital dynamics α=0.4 e) Orbital dynamics l α=0.6 f) orbital dynamics α=0.8

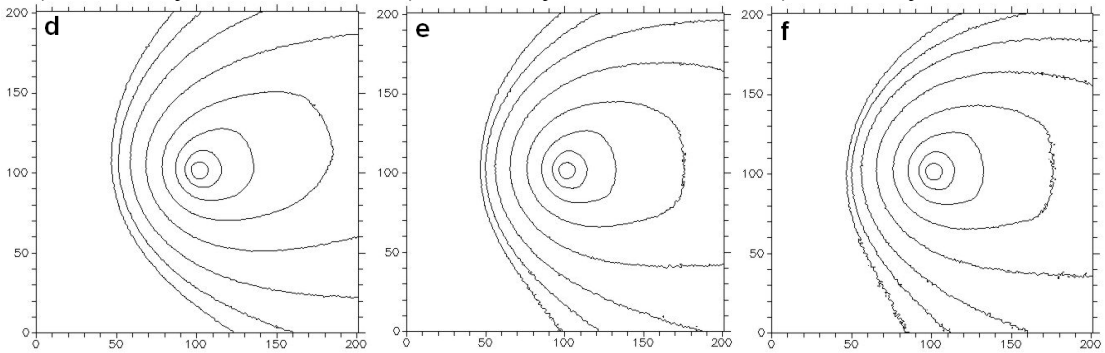

Foster and Green Fig 8

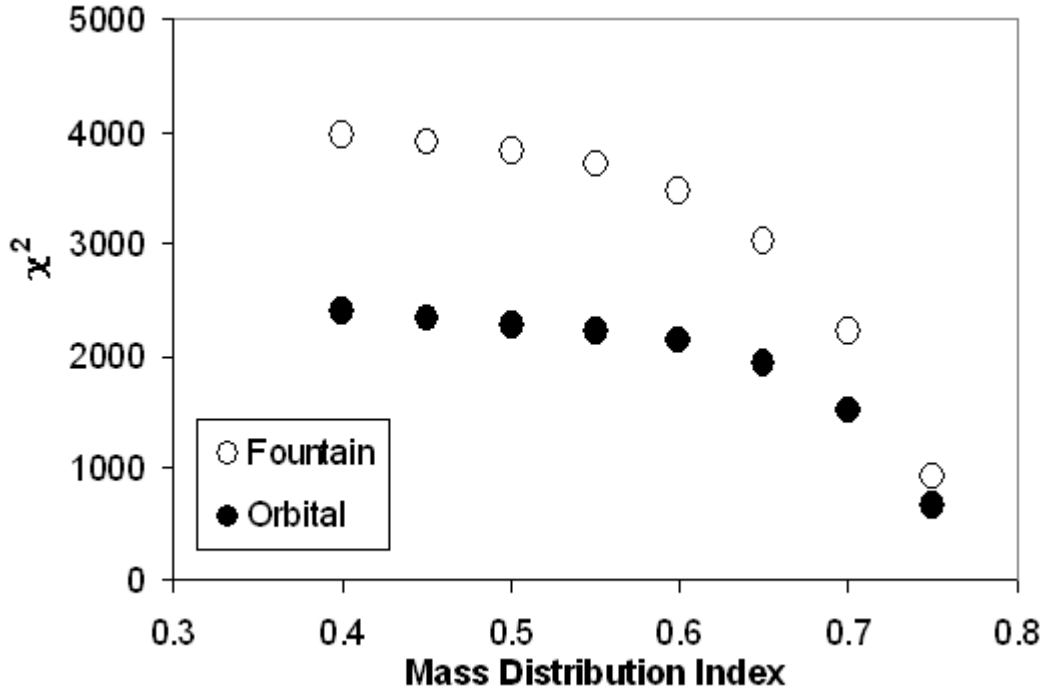

Foster and Green Fig 9

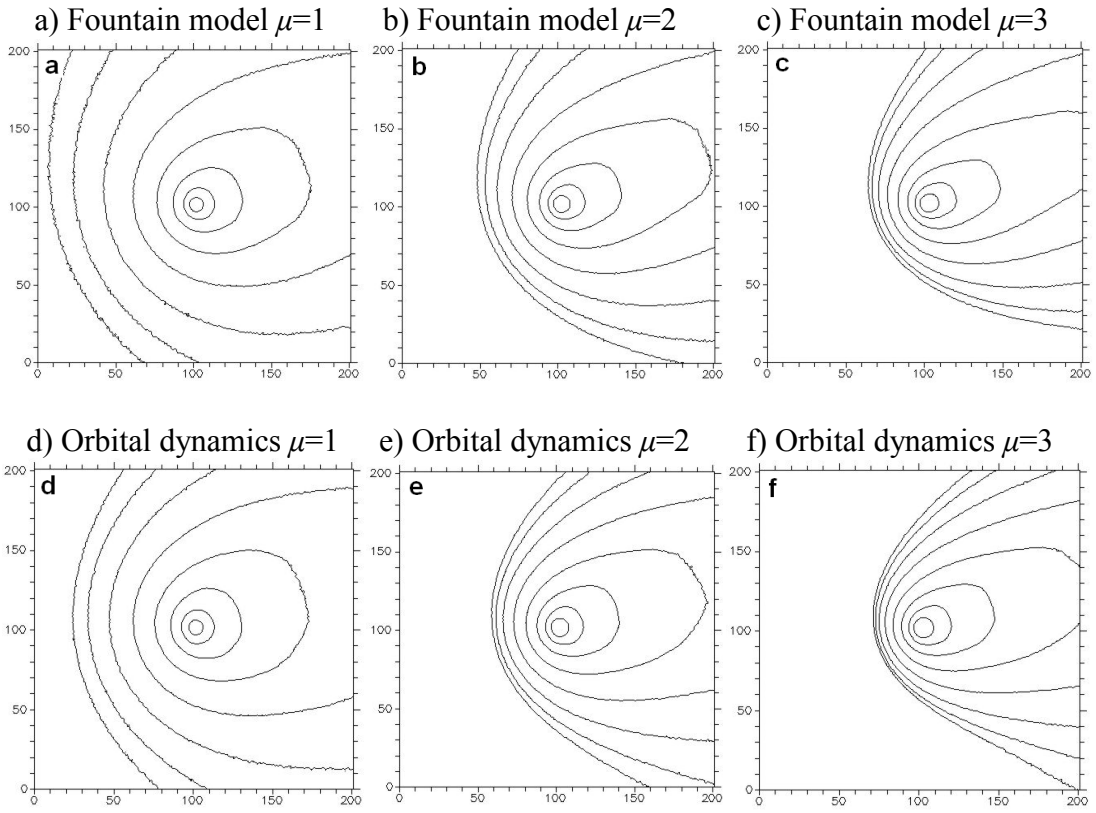

Foster and Green Fig 10

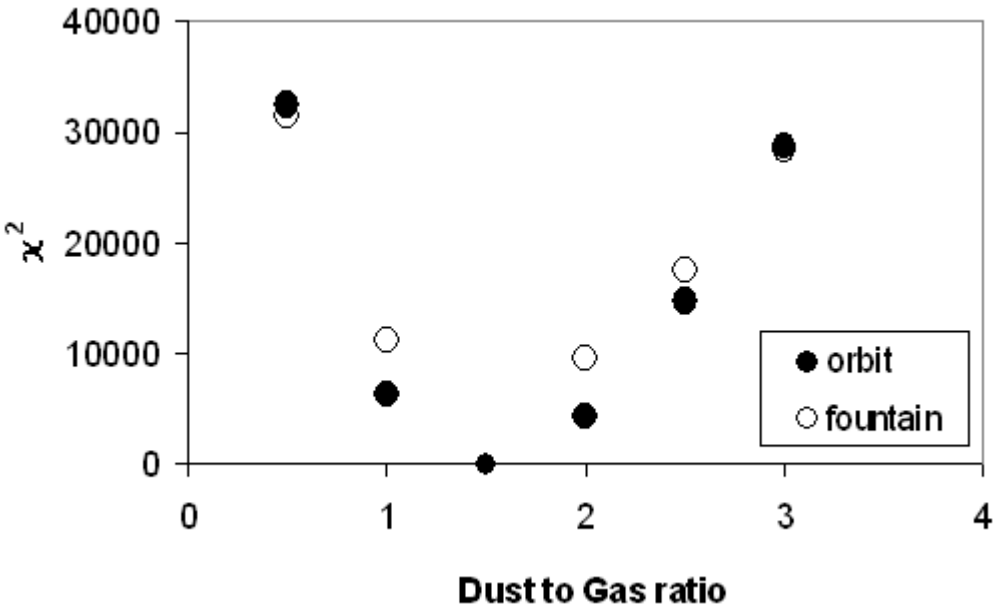

Foster and Green Fig 11

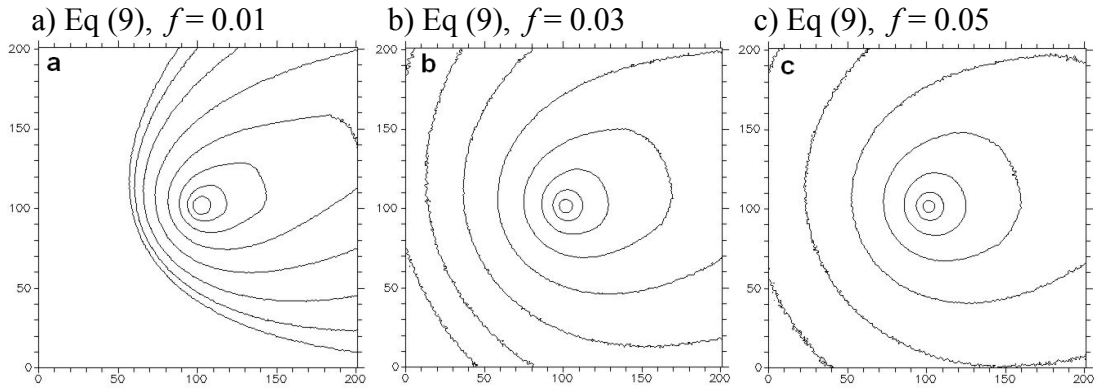

Foster and Green Fig 12

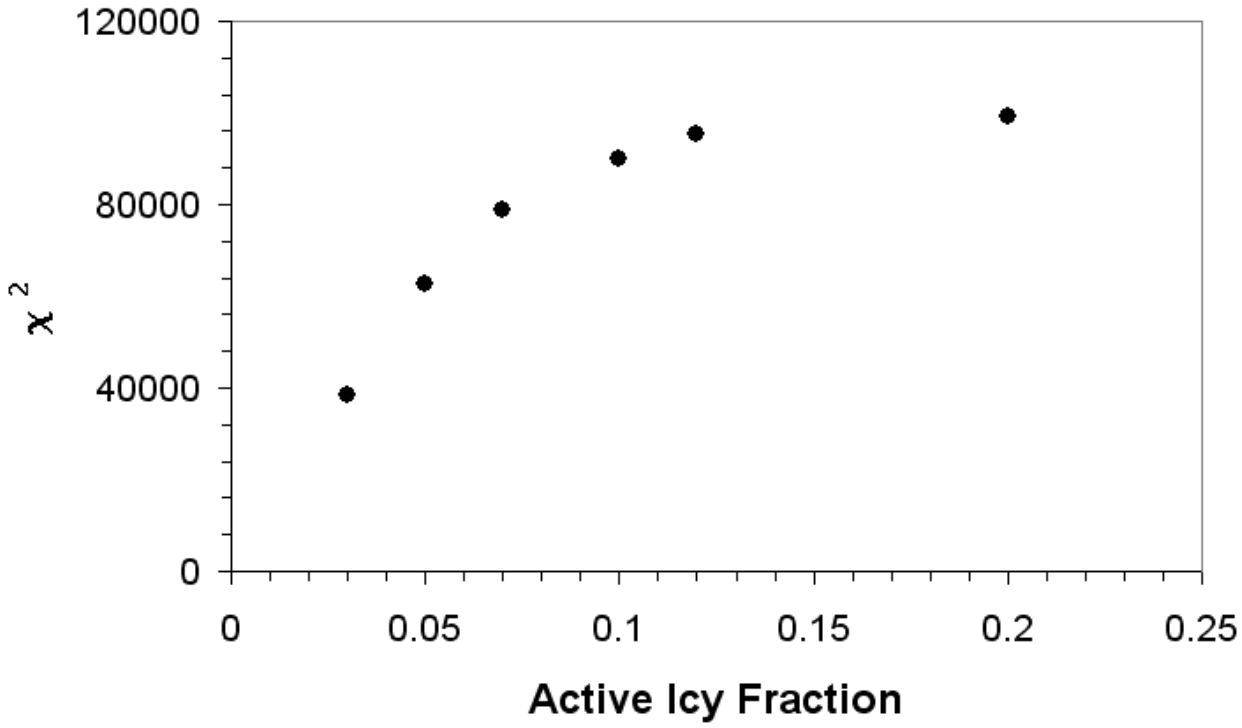

Foster and Green Fig 13

a) $\cos^2(\theta)$ b) $\cos^2(\theta/2)$ c) $5 - 3\cos(\theta)$

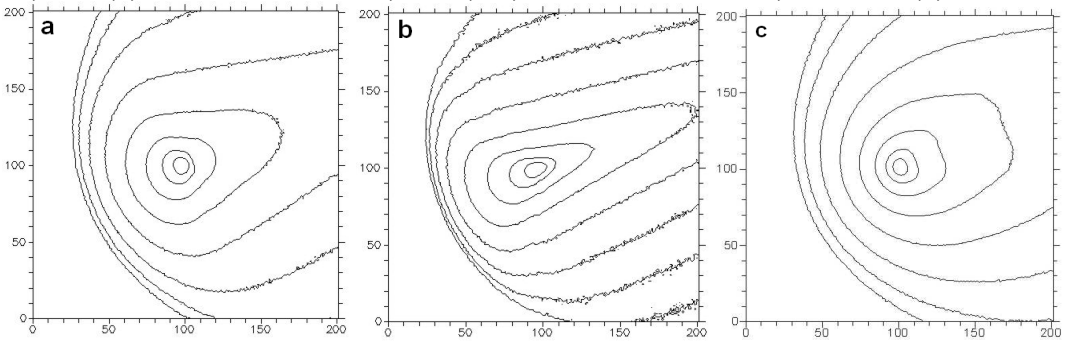

Foster and Green Fig 14

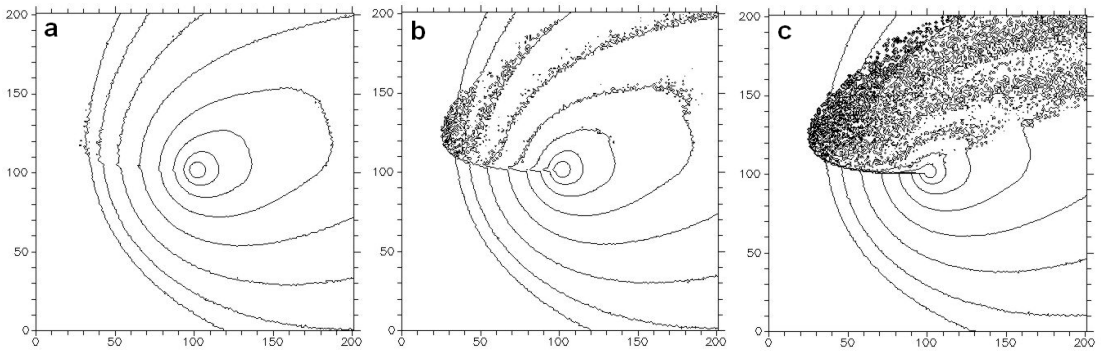

Foster and Green Fig 15

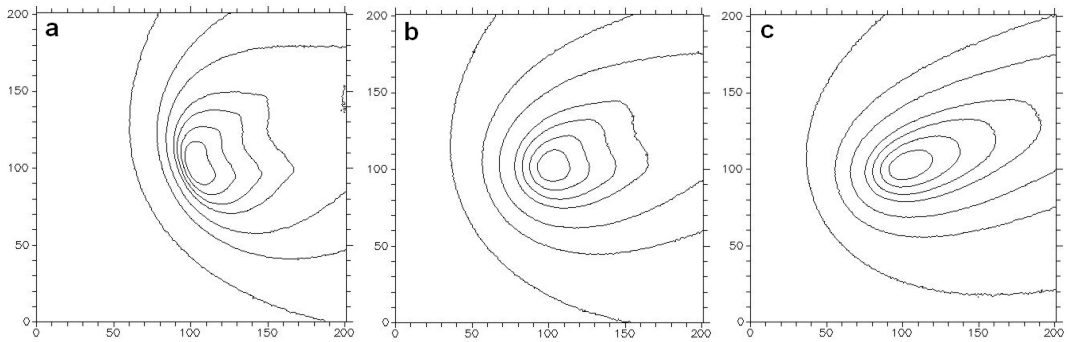

Foster and Green Fig 16

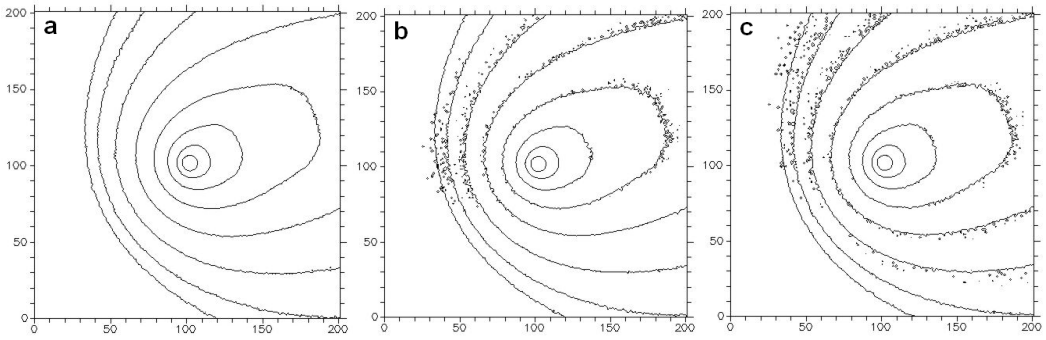

Foster and Green Fig 17

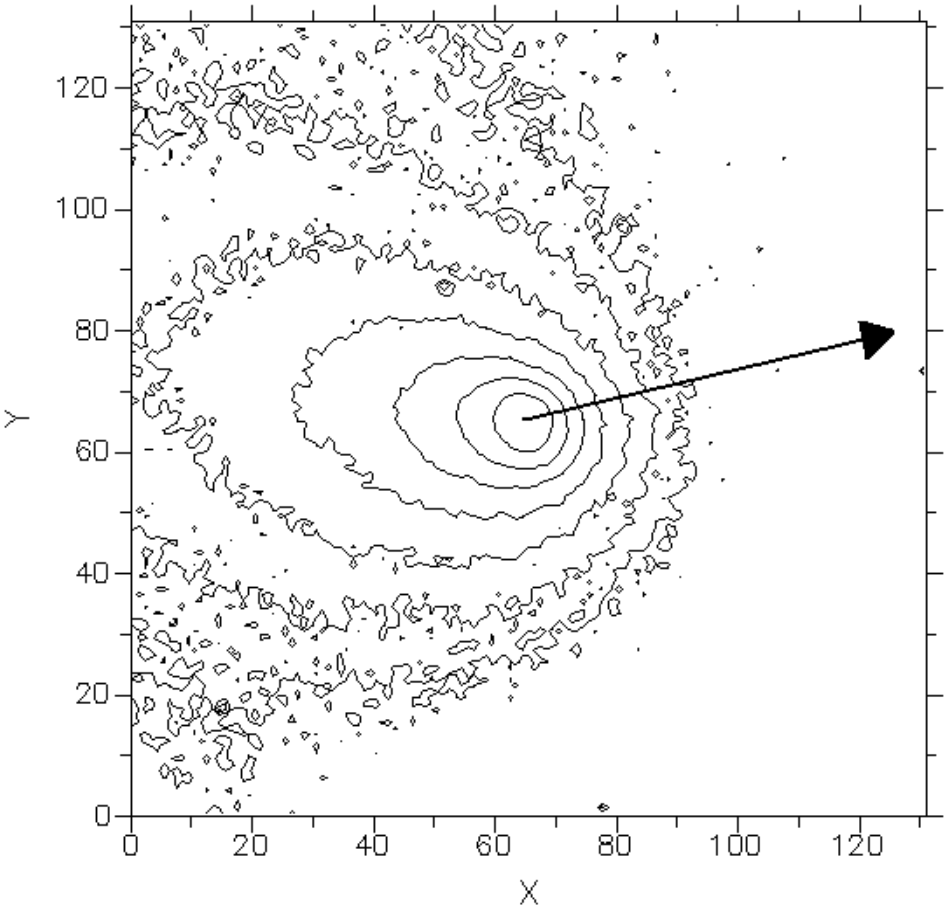

Foster and Green Fig 18

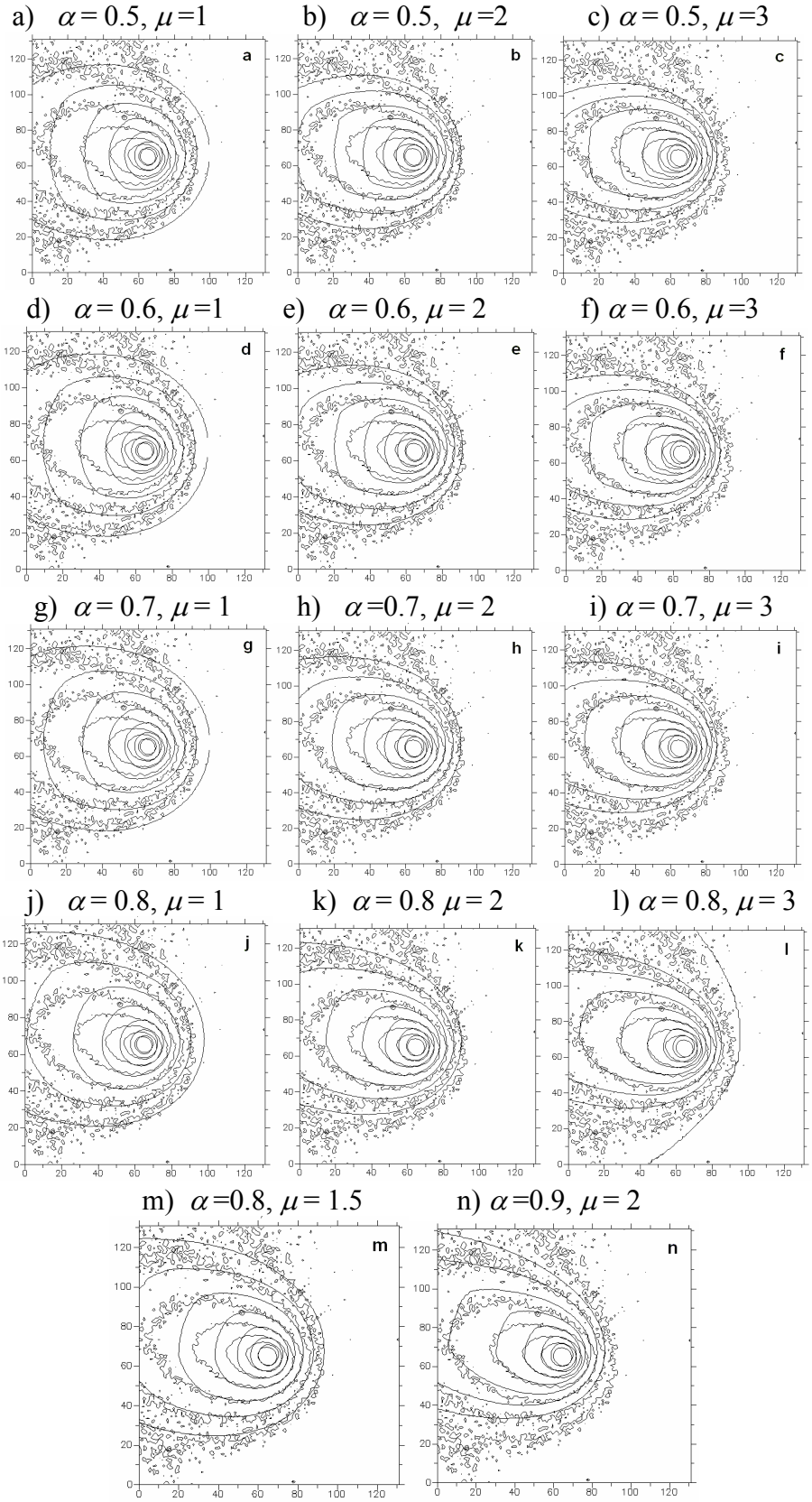

Foster and Green Fig 19

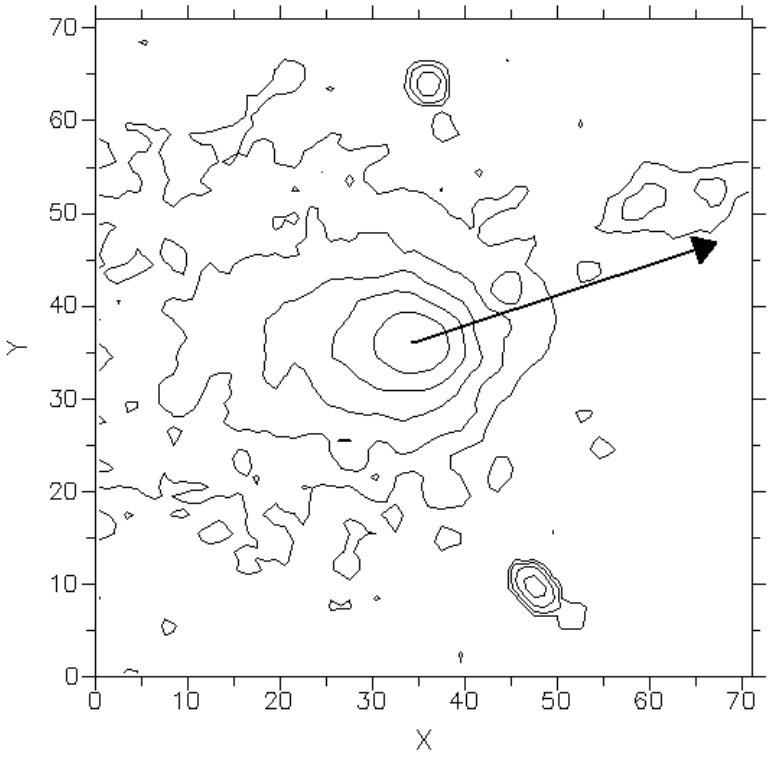

Foster and Green Fig 20

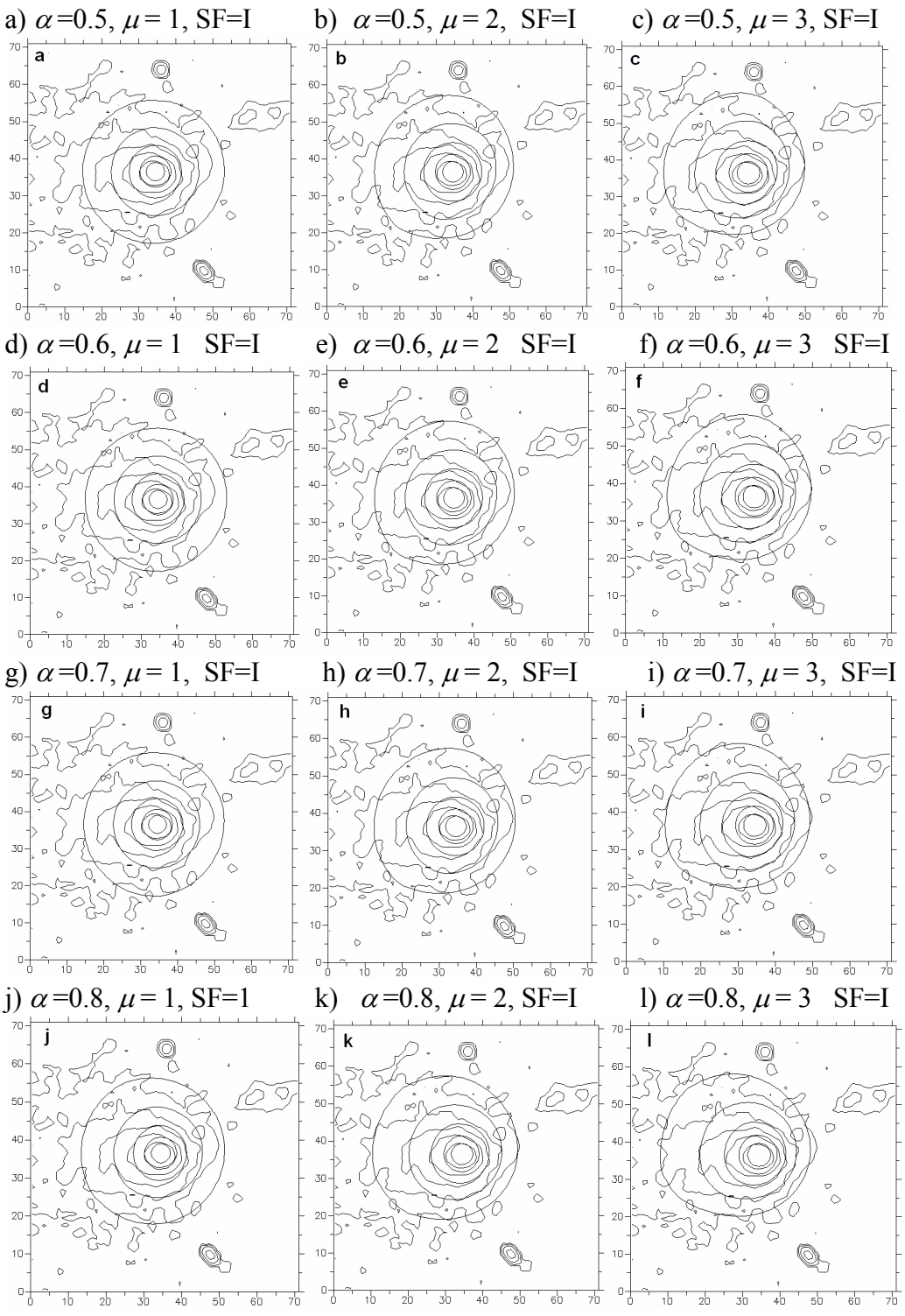

m) α=0.7, μ= 5.5, SF= 0.75 +3 cos θ

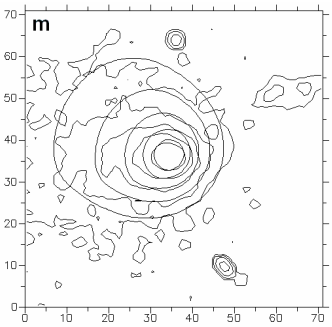

n) α=0.8, μ= 5.5, SF= 0.75 +3 cos θ

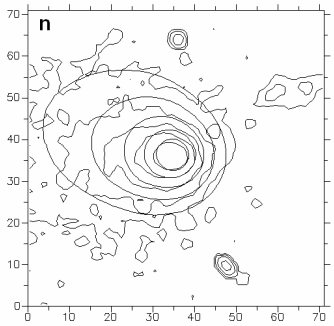

o) α=0.9, μ= 5.5, SF= 0.75 +3 cos θ

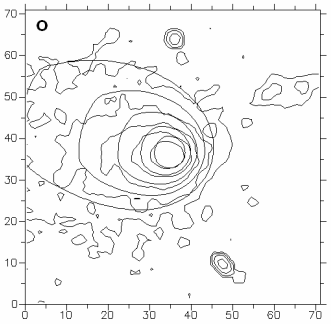

p) α=0.7, μ= 5.5, SF= 0.5 + 2 cos θ

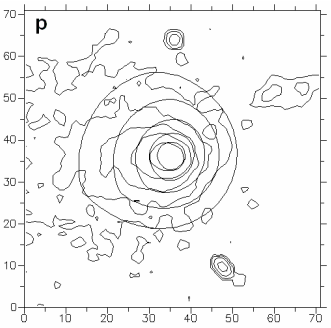

q) α=0.8, μ= 5.5, SF= 0.5 + 2 cos θ

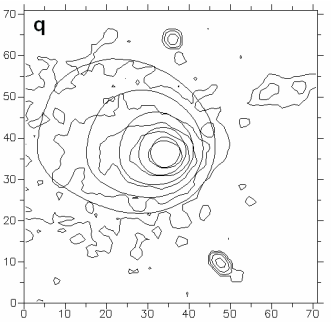

r) α=0.9, μ= 5.5, SF= 0.5 + 2 cos θ